Flux of light antimatter nuclei near Earth, induced by cosmic rays in the Galaxy and in the atmosphere

R. Duperray,[1] B. Baret,[1] D. Maurin,[2] G. Boudoul,[1,*] A. Barrau,[1] L. Derome,[1] K. Protasov,[1] and M. Buénerd[1,†]

[1]*Laboratoire de Physique Subatomique et de Cosmologie, CNRS/IN2P3, 53 avenue des Martyrs, 38026 Grenoble-cedex, France*

[2]*Service d'Astrophysique, SAp CEA-Saclay, F-91191 Gif-sur-Yvette CEDEX, France*

(Received 18 November 2004; published 26 April 2005)

The fluxes of light antinuclei $A \leq 4$ induced near Earth by cosmic ray interactions with the interstellar matter in the Galaxy and with the Earth's atmosphere are calculated in a phenomenological framework. The hadronic production cross section for antinucleons is based on a recent parametrization of a wide set of accelerator data. The production of light nuclei is calculated using coalescence models. For the standard coalescence model, the coalescence radius is fitted to the available experimental data. The nonannihilating inelastic scattering process for the antideuterons is discussed and taken into account for the first time via a more realistic procedure than used so far for antiprotons.

DOI: 10.1103/PhysRevD.71.083013 PACS numbers: 98.35.Pr, 95.30.Cq, 96.40.−z, 98.70.Sa

I. INTRODUCTION

Antiprotons in cosmic rays (CR) have been extensively studied both experimentally and theoretically over the last few decades, with the general purpose of measuring their flux and understanding their origin. It is now generally agreed that the dominant part of the $\bar{p}$ CR spectrum is a secondary flux originating from the hadronic production induced by CRs on the interstellar (IS) medium (ISM). This agreement is grounded on the ability of the calculations based on this assumption to reproduce the data. Recently some new prospects have been outlined, strengthening the motivations for the study of the $\bar{p}$ flux [1], and extending the interest for CR antimatter to other light antinuclei, antideuterons $\bar{d}$ in particular, with the emergence of new astrophysical issues. The $\bar{p}$ and $\bar{d}$ production in neutralino annihilation has been considered as a possible signature for the dark matter constituents in the Universe [2]. Antiprotons and antideuterons have also been considered as evaporation products of primordial black holes (PBH) and their flux at Earth calculated in the perspective of searching for a possible signature of the source in the experimental spectra [3,4]. A common feature of these studies is that the calculated fluxes are extremely small in intensity with their spectra peaked at low momenta. This requires the secondary galactic contribution to be accurately known for a significant search of the former to be considered.

Another motivation for a careful examination of the antimatter production in the Galaxy is provided by the need for evaluating the galactic flux which will constitute a physical background for the forthcoming new experiments to search for primordial antimatter in the Universe [5–8]. The evaluation can be performed using the CR flux data from the latest generation of experiments [5,9,10].

In the atmosphere, the CR induced $\bar{p}$ flux has been measured recently [11] at mountain altitude, and some antinuclei production is naturally expected to originate from the same source. These atmospheric secondaries will generate another physical background in future experiments. Although it could be separated, in principle, from the galactic flux on dynamic and kinematic grounds, a soundly based knowledge of this background is required. Recently the phenomenology of the particle production induced by CRs in the atmosphere has been thoroughly investigated with the purpose of accounting for the large amount of new data available from recent balloon and satellite measurements [12,13]. For the $\bar{p}$ flux, it has been shown in these works that this flux can be accounted for in a conceptually simple, albeit numerically elaborated, framework [12,13]. These calculations are extended here to the case of $A > 1$ antinuclei.

The primary purpose of the present study is to calculate the flux of antimatter particles of galactic and atmospheric origin, anchoring them as firmly and as widely as possible in the existing body of experimental data. The galactic and atmospheric production of $\bar{p}$ and $\bar{d}$, as well as $\bar{t}$, $^3\bar{\mathrm{He}}$, and $^4\bar{\mathrm{He}}$, and their flux in orbit near Earth can be evaluated at a so far unmatched level of confidence by using the available hadronic production data for these particles on the one hand, and the proven coalescence model on the other hand. A few preliminary steps of this work have been covered already and published: The systematics of the $\bar{p}$ data over a wide range of incident momentum has been recently gathered and reanalyzed [14], providing an accurate parametrization of the inclusive antiproton production cross section. The first calculations of the atmospheric $\bar{p}$ flux were reported in [13]. Other steps dealing with the coalescence models are quoted below. In addition, some important aspects of

*Permanent address: IPNL, Université Claude Bernard, 4 rue E. Fermi, 69622 Villeurbanne-cedex, France

†Corresponding author: buenerd@lpsc.in2p3.fr

the production mechanisms of light composite nuclei and antinuclei relevant to the study are available from high energy heavy ion physics data, strengthening its grounds: a key point is that the deuteron coalescence parameter derived from empirical fits to the data has been found to be energy independent to within a few tens of percents, through a wide incident energy range including the range of interest here, for pA systems (see [15,16], for example, and below). This feature is expected to be valid for antideuteron coalescence as well, on general theoretical grounds. It is also supported by experimental indications [17–19].

The rescattering on the ISM (or on the atmospheric nuclei) of the secondary particles in the propagation, and the contribution of this process to the low momentum flux of CR particles are important aspects of the calculations since several fluxes of primary origin and of major astrophysical interest are expected to contribute to the low momentum range, where the knowledge of the secondary flux has to be most accurate. The issue has been addressed in this work, with the same concern of keeping as close as possible to the experimental facts as well as following general principles. It is discussed in a dedicated section and appendix below. The subject of $\bar{d}$ rescattering has been addressed previously in Ref. [20].

Finally, whereas the atmospheric antinuclei fluxes depend mostly on the proton and helium fluxes at the top of atmosphere (TOA), which are well measured, the galactic secondary antinuclei fluxes must be evaluated by means of a propagation model. Two classes of such models are widely used. The simplest one is the popular leaky box model (LBM), whereas a more realistic approach is the two-zone diffusion model (DM) [1]. In the former, all the details about the transport conditions are discarded. These are globally accounted for by one single parameter, the confinement time of cosmic rays in the Galaxy, which, once fixed, leads to a balance between the production of secondary species (LiBeB, $Z = 21$–23) from their respective primary parents (CNO, Fe) and the escape from the Galaxy, to reproduce the data [21]. This model gives correct results for the particle fluxes of stable nuclear species.

The paper is organized as follows. The hadronic production cross sections and the coalescence model are discussed in Sec. II. The total reaction cross sections used in the calculations for the antimatter absorption are presented in Sec. III A, with the particles rescattering issue treated in Sec. III B. The antimatter propagation is discussed in Sec. IV, while the atmospheric production is presented in Sec. V. The results are discussed and the work is briefly concluded in Sec. VII. Some details on the physics of the rescattering process are given and discussed in the appendix.

II. ANTIMATTER NUCLEI PRODUCTION CROSS SECTIONS

A. Production mechanism and coalescence process

1. The standard coalescence model

In the standard coalescence model, the invariant differential cross section for the (inclusive) production of composite fragments with nuclear mass number A, is related to the inclusive production cross section of nucleons by a simple power law [22]:

$$\left(E_A \frac{d^3N_A}{d\vec{p}_A^{\,3}}\right) = B_A \cdot \left(E_p \frac{d^3N_p}{d\vec{p}_p^{\,3}}\right)^A, \tag{1}$$

where N_A and N_p are the A nucleus and nucleon production multiplicities, respectively, and with $\vec{p}_A = A \cdot \vec{p}_p$. The coalescence coefficient B_A can be expressed in terms of the coalescence momentum p_0 and of the nuclear characteristics of the colliding system.

In the case of deuteron or antideuteron coalescence out of matter-antimatter production, B_A is defined by the relation giving the probability of finding a neutron and a proton within p_0 distance in the momentum space [22,23], which leads to

$$\gamma \frac{d^3N_d}{d\vec{p}_d^{\,3}} = \frac{4\pi}{3} p_0^3 \left(\gamma \frac{d^3N_p}{d\vec{p}_p^{\,3}}\right)\left(\gamma \frac{d^3N_n}{d\vec{p}_n^{\,3}}\right) \tag{2}$$

where γ is the Lorentz factor. The multiplicity for particle i is

$$\frac{d^3N_i}{d\vec{p}_i^{\,3}} = \frac{1}{\sigma_R} \frac{d^3\sigma_i}{d\vec{p}_i^{\,3}}$$

where σ_R is the total nucleon-nucleus reaction cross section. Assuming equal neutron n and proton p production cross sections and momentum distributions, the relation can be approximated as

$$\gamma \frac{d^3N_d}{d\vec{p}_d^{\,3}} = \frac{4\pi}{3} p_0^3 \left(\gamma \frac{d^3N_p}{d\vec{p}_p^{\,3}}\right)^2. \tag{3}$$

This relation can then be straightforwardly extended to the coalescence of A nucleons as [23]

$$\gamma \frac{d^3N_A}{d\vec{p}_A^{\,3}} = \left(\frac{4\pi}{3} p_0^3\right)^{(A-1)} \left(\gamma \frac{d^3N_p}{d\vec{p}_p^{\,3}}\right)^A. \tag{4}$$

Finally, the coalescence coefficient deduced from relations (1) and (4) above is given by

$$B_A = \left(\frac{4\pi}{3} p_0^3\right)^{(A-1)} \frac{m_A}{m_p^A}. \tag{5}$$

The inputs for the calculation of the production cross section for mass A nuclei (antinuclei) then consist only of the value of the B_A ($B_{\bar{A}}$) parameter, the proton (antiproton) production differential cross section, and the total pp reaction cross section σ_R.

As quoted in the introduction, the deuteron coalescence momentum or coalescence radius (see Ref. [23], for example, for the definitions) derived from empirical fits to the

data has been found to be practically energy independent between a few hundred MeV per nucleon and 158 GeV per nucleon incident kinetic energy (see, e.g., [15,16,24–29] for more detailed studies), as expected from the simple coalescence model [22]. The property seems to hold as well for mass 3 nuclei and for ^{4}He [25]. The $B_{A=2}$ and $B_{A=3}$ coalescence parameters for p induced collisions on nuclei can thus be taken constant over this range.

In the simple coalescence model successfully describing the light nuclei production in pA and AA collisions at low and intermediate energies, the coalescence nucleons originate from the excited nuclear matter of the target (projectile) nucleus, and coalescence particles are produced in the target (projectile) rapidity range. In the case of high energy pp collisions, nucleon-antinucleon pairs originating from the hadronization process are produced in the nucleon-nucleon (NN) center of mass (cm) rapidity region. The coalescence nuclei originate from these hadronization products whose production cross section is maximum at rest in the cm and which therefore fly in the laboratory frame with the cm velocity. In these collisions, the rapidity distributions of the produced particles is thus symmetric with respect to the cm rapidity [15,19,30–32]. In high energy AA collisions, both mechanisms are allowed; the rapidity distributions of light nuclei produced by nuclear coalescence of target nucleons are centered around the target rapidity, i.e., in the low momentum region in the laboratory frame for fixed target experiments, and symmetrically around the projectile rapidity (see [19] for example). In these collisions, the coalescence production from single NN collisions is also expected to exist, with a much lower cross section however.

There are therefore two sources of coalescence nucleons, produced in very different dynamical regimes: one is the production out of excited nuclear matter; the other is the production out of hadronization products from individual NN collisions. The coalescence model which applies well to the first case does not necessarily apply to the second. In this latter reaction however, the measured d and $\bar{d}$ production cross sections have both been shown to be consistent with a coalescence production mechanism as for nuclear systems [33–37], which indicates that the same approach can be used both for matter and antimatter production calculation.

In addition, the similarity of the production mechanism for light nuclei and antinuclei was also suggested by various experimental indications in AA collisions. In this case, however, the coalescence parameter was found to be incident energy dependent [15–18,38]. Note that the microscopic approach to the coalescence model was developed initially [39] to explain this dependence of the coalescence parameter on the kinematic conditions of the reaction. For $p + A$ systems, however, the coalescence coefficients were found to be energy independent as mentioned above, for d as well as for $\bar{d}$ [15,16,31]. This will be confirmed below for $\bar{d}$ particles.

These observed dynamical and kinematical features allow us therefore to make reliable predictions for the production in space of light antimatter nuclei from AA collisions (A standing here for any nucleus including proton), over a range of incident CR proton energies conveniently matching the useful range for the present study.

2. Microscopic coalescence model

A microscopic approach to the coalescence model has been developed recently in [39,40], which successfully described the mass 2 and 3 antinuclei production $pA \rightarrow \bar{d}X$ and $pA \rightarrow \bar{3}X$ ($\bar{3}$ standing for $\bar{t}$ and $^3\bar{\text{He}}$) experimental data. The model has been used in the present work as a complementary tool to the standard coalescence model.

The two models have been used in the study in order to provide an estimate of the theoretical uncertainty to be assigned to the calculations. This uncertainty was turned around however by the standard model being fitted to the available data.

B. Antiproton production cross section

The cross section data for the proton induced inclusive $\bar{p}$ production on nuclei and on the nucleon have been reanalyzed recently, in the framework of a research program aiming at the understanding of the secondary particle flux produced in the atmosphere [13]. This was achieved using an improved analytical form used in previous works for fitting the cross sections [14], and it was shown that the data could be described with a fair accuracy over the incident energy range between 12 and 400 GeV. The results of this work, i.e., for $pA \rightarrow \bar{p}X$ and $pp \rightarrow \bar{p}X$ cross sections, have been used in the present calculations, and the relevant part for the present study is repeated here for convenience.

The parametrization of the inclusive $pA \rightarrow \bar{p}X$ cross section data is one of the two major ingredients of the present calculations, on which results and conclusions are built. The $pA \rightarrow \bar{p}X$ cross sections obtained from the analysis of [14] are estimated to be accurate to within about 20% above $T_{\bar{p}} \approx 1$ GeV. The low kinetic energy $\bar{p}$ data 0.5 GeV $\lesssim T_{\bar{p}} \lesssim 1$ GeV are probably less accurate. They tend to be somewhat underestimated by the analytical form used [14]. No fully reliable estimate of the low energy $T_{\bar{p}} \lesssim 0.4$–0.5 GeV accuracy can be assessed because of the total lack of data over this range and of the high sensitivity to nuclear medium effects. Symmetry considerations also constrain the low energy data (see the discussion in [14]) for the pp system. Unfortunately, these cannot be fully applied to the pA data because of the nuclear medium effects on the final state in the $\bar{p}$ production, which may more than significantly distort the spectrum. This issue would deserve a dedicated study by itself. For the $pp \rightarrow \bar{p}X$ cross section, two versions of the parametrization are available: the $A = 1$ version of the pA parametrization (below referred to as I) , and a dedicated

simplified version of the formula with no nuclear mass dependence in the analytical form, which provides a markedly better fit to the $\bar{p}$ production in pp collisions data (below referred to as II). The two versions provide values of the integrated cross sections (multiplicity) differing by about 20%, the $[pA \rightarrow \bar{p}X]_{A=1}$ fit (I) providing the larger values. Both parametrizations have been used in the present work for the pp cross sections.

C. Antideuteron production

Galactic antideuterons are expected to be produced in pA and AA collisions dominantly by the elementary $pN \rightarrow \bar{d}X$ process via a coalescence mechanism out of the hadronic production of $N\bar{N}$ pairs as discussed previously. Another competing production is possible however in space, from the $\bar{p}p \rightarrow \bar{d}X$ reaction. This reaction has to be considered since although the $\bar{p}$ flux is much lower than the p flux, only one $N\bar{N}$ pair has to be produced in the kinematical domain where the "incident" $\bar{p}$ in the final state can coalesce with a $\bar{n}$ particle produced in the collision, providing a lower energy $\bar{d}$ flux than the other reaction but with a comparable magnitude. Both production channels are discussed in the next two subsections.

1. Antideuteron production in the $pA \rightarrow \bar{d}X$ reaction

The simple coalescence model described above has been applied to a set of antideuteron cross section production data available in the literature [28,29,34,36]. Figure 1 shows the results obtained using the coalescence formula (4) with the $\bar{p}$ spectra obtained as in [14], and fitting the value of the coalescence momentum to a selected sample of data, with the result $p_0 = 79$ MeV/c. As seen on the figure the data are well reproduced by the calculations over a range extending from 200 GeV/c incident momentum up to the ISR cm energy $s^{1/2} = 53$ GeV. In total 34 data points have been fitted. The results are given in Table I.

TABLE I. Experimental $\bar{d}$ production cross section data used in the coalescence model analysis to fit the coalescence momentum parameter as discussed in the text. N is the number of experimental points used in the fit.

Experiment	Target	$p_{\rm inc}$ or $\sqrt{s}$	N	χ^2/N
		GeV/c GeV		
Bussière *et al.* [28]	Be	200	5	0.95
	Al	200	3	1.7
Cronin *et al.* [29]	Be	300	1	4.4
	Ti	300	1	1.3
	W	300	4	13.7
Alper *et al.*; Gibson *et al.* [36]	p	$\sqrt{s} = 53$	8	1.3
Albrow *et al.* [35]	p	$\sqrt{s} = 53$	3	1.0
Armitage *et al.* [41]	p	$\sqrt{s} = 53$	9	4.6

The 70 GeV data from Refs. [27,42] have been discarded from the search. They were found not to be compatible with the other data, since they provided exceedingly large χ^2 values. These data are listed in Table II. It is seen in the table that the data measured on the Pb target have a not so bad χ^2 per point value (bottom line in the table). They have

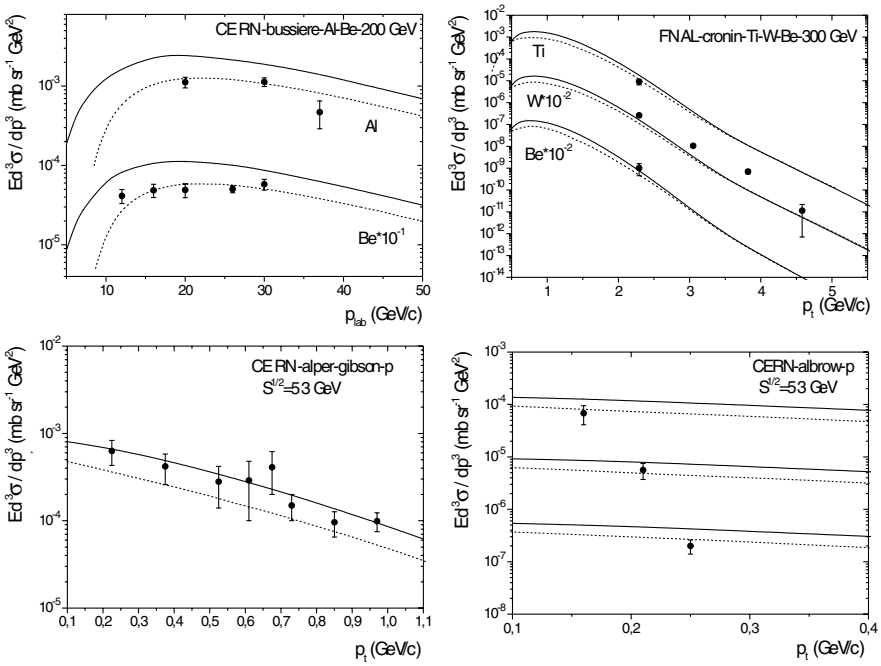

FIG. 1. Comparison of the deuteron production cross section calculated with the standard (dashed lines) and microscopic (solid lines) coalescence models, with the experimental data from pA collisions at lab momenta 200 GeV/c on Be and Al targets (top left) [28], at 300 GeV/c on Be, Ti and W targets (top right) [29], and at 53 GeV center of mass energy on the proton from [36] (full circles) and [34] (open circles, bottom left), and from [35] (bottom right).

TABLE II. Experiments whose results were not included in the search. The chi-squared per point values (rightmost column) were obtained using the coalescence parameters fitted to the selected data listed in Table I. Same definitions as in previous table.

Experiment	Target	$p_{\rm inc}$	N	χ^2/N
		(GeV/c)		
Binon *et al.*; Antipov *et al.* [42]	Al	70	6	2.10^4
Abramov *et al.* [27,37]	p	70	2	1.10^3
	Be	70	3	3.10^2
	Pb	70	4	15.4

not been used in the analysis, however, for the sake of consistency. Although the observed disagreement could be of physical origin since the discarded data have been measured at an incident energy below the momentum range of good agreement in Fig. 1, they have not been treated on the same footing as the other data because the $\bar{p}$ yields measured in the same set of experiments were already found to be inconsistent with the measurements from other works [14]. The comparison of these data with the standard coalescence model calculations using a coalescence parameter fitting the data sets listed in Table I are shown in Fig. 2. The disagreement clearly varies from moderate to sharp, with no clear trend pointing to some possible physical origin. The data are very overestimated or very underestimated by the calculations for the same incident energy for the different measurements. In the calculations of the $\bar{d}$ and $\bar{3}$ yields, the threshold effects were taken into account by means of the phase space of the final state as described in Ref. [40].

2. Antideuteron production in the $\bar{p}A \rightarrow \bar{d}X$ reaction

For the antideuteron production calculation in the $\bar{p}p(\mathrm{He}) \rightarrow \bar{d}X$ reaction(s) either in the simple or in the microscopic, coalescence model, the inclusive $\bar{p}$ production cross section from the same incoming channel is needed. Since this cross section is unknown experimentally, an evaluation procedure has been used to estimate it on the basis of reliable approximations. In the assumed production mechanism, the $\bar{p}p \rightarrow \bar{d}X$ reaction produces one single $N\bar{N}$ pair out of which the $\bar{n}$ (antineutron) will coalesce with the "existing" $\bar{p}$ in its final state, into a $\bar{d}$, i.e., $\bar{p}p \rightarrow (\bar{p}\,\bar{n})npX \rightarrow \bar{d}X$. The following assumptions

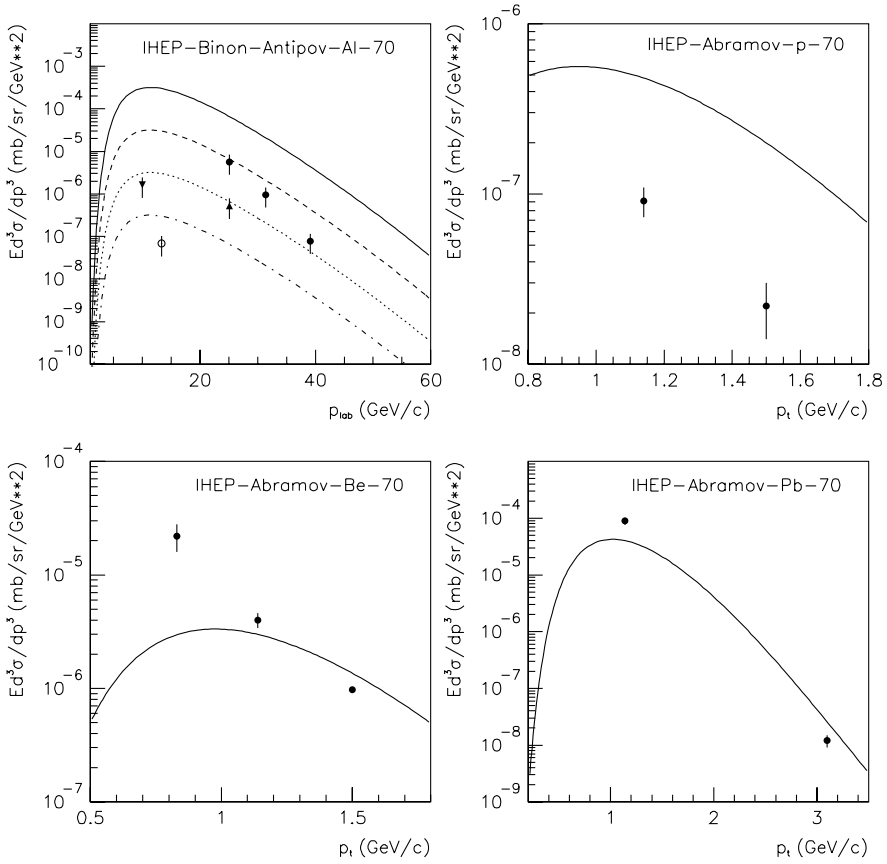

FIG. 2. Comparison of the antideuteron production cross section calculated with the standard coalescence model as described in the text, with the inclusive experimental data from pA collisions at 70 GeV/c from Refs. [27,37,42]. The upper left frame shows the data measured at a set of angles, 0° (full circle, solid line), 12 mrad (inverted triangle, dashed line), 27 mrad (full triangle, dotted line), and 47 mrad (open circle, dash-dotted line). See text for details.

based on the knowledge of the $\bar{p}p \to \bar{p}X$ and $\bar{p}p \to \bar{n}X$ processes have been made for this evaluation:

(1) The probability to produce an antiparticle by hadronization in a $\bar{p}p$ collision $\bar{p}p \to \bar{n}X$ in the final state energy range of interest, i.e., excluding the quasielastic charge exchange processes to the resonance region, is the same as the probability to produce a $\bar{p}$ in a pp collision $pp \to \bar{p}X$:

$$E_{\bar{n}}\frac{d^3\sigma_{\bar{n}}}{d^3p_{\bar{n}}}(\bar{p}p \to \bar{n}X) \approx E_{\bar{p}}\frac{d^3\sigma_{\bar{p}}}{d^3p_{\bar{p}}}(pp \to \bar{p}X).$$

For the $\bar{p}p(\mathrm{He}) \to \bar{n}X$ inclusive cross section, parametrizations II and I were used for pp and pHe collisions, respectively.

(2) The $\bar{p}p \to \bar{p}X$ cross section is assumed to be the same as the $pp \to pX$ cross section, namely,

$$E_{\bar{p}}\frac{d^3\sigma_{\bar{p}}}{d^3p_{\bar{p}}}(\bar{p}p \to \bar{p}X) \approx E_{\bar{p}}\frac{d^3\sigma_{\bar{p}}}{d^3p_{\bar{p}}}(pp \to pX).$$

This approximation makes sense since the collision dynamics are similar for the two systems at high enough collision energies. It is probably not correct however for low energy secondary $\bar{p}s$ from nuclear targets because of the dominance of the annihilation cross section in $\bar{p}N$ collisions at these energies and of the subsequent interactions of the produced $\bar{p}s$ with the nuclear medium. For the proton inclusive cross section, the parametrization from [43] has been used.

An additional correction has to be made for the energy dependence of the $\bar{d}$ production cross section near the threshold, assumed to follow the phase space available to the particle [40].

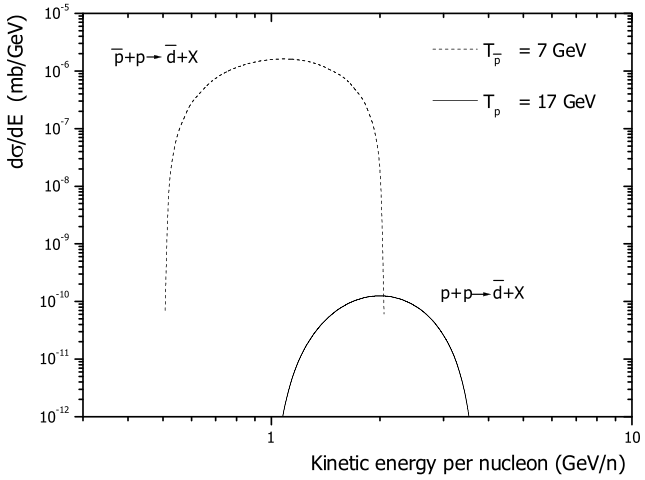

FIG. 3. Spectral distribution of the antideuteron production cross section in the two reaction schemes $pp \to \bar{d}X$ (solid line) and $\bar{p}p \to \bar{d}X$ (dashed line) considered, calculated with the standard coalescence model as described in the text. $T_{\bar{p}}$ and T_p are the production thresholds.

The differential cross sections for the $pp \to \bar{d}X$ and $\bar{p}p \to \bar{d}X$ reactions calculated using the coalescence model(s) are compared in Fig. 3 for incident energies near their respective threshold. For the latter reaction, the calculation was performed within the approximations described above. It can be seen in the figure that the $\bar{p}p \to \bar{d}X$ cross section is much larger than for the $pp \to \bar{d}X$ reaction, the maximum values being about 4 orders of magnitude apart. The distributions are also centered at very different particle energies, corresponding to the respective NN center of mass velocities in both cases, and being thus much lower for the $\bar{p}p \to \bar{p}p(\bar{n}n)$ reaction than for the $pp \to pp(\bar{p}p)(\bar{n}n)$ reaction. These features clearly show that the $\bar{p}p \to \bar{d}X$ contribution has to be taken into account in the calculations of the galactic $\bar{d}$ flux.

D. Mass 3 and 4 antinuclei production cross section

The production cross sections of mass 3 antinuclei ($\bar{t}$, $^3\bar{\mathrm{He}}$) in pA collisions are extremely scarce. They have been measured in the past only at 70 GeV [44,45], and at 200 and 240 GeV [28].

In the Serpukhov experiments [44,45], the $\bar{t}$ and $^3\bar{\mathrm{He}}$ production cross sections have been measured at small production angles on Be and Al targets. The $\bar{p}$ and $\bar{d}$ data from the same series of experiments have been discarded from the sets of data fitted in the present analysis, as discussed previously. For the results of the mass 3 antinuclei production cross section measured in these experiments, no consistent interpretation could be found either [46], albeit the standard coalescence calculations are found in reasonable agreement with the data, i.e., typically less than 1 order of magnitude larger.

The production cross sections of mass 3 antinuclei have also been measured at CERN in a series of two experiments [28]. The measured $\bar{p}$ and $\bar{d}$ cross sections have been discussed in the previous subsection. The mass 3 data are compared in Fig. 4 to the calculated cross sections in the coalescence models. The calculated cross sections are found within 1 order of magnitude from the data points for the two studied targets, with the two coalescence models providing values approximately framing the data points, the microscopic model providing the upper limit. This agreement can be considered as fair as far as the order of magnitude is concerned. It is quite a significant result for the present study whose purpose is to fix the orders of magnitude of the corresponding secondary CR flux. It is interesting to note in the figure that the experimental production cross section is found significantly larger for $\bar{t}$ than for $^3\bar{\mathrm{He}}$ for all values of momenta where both have been measured. Should this difference be assigned to Coulomb effects in the coalescence process is an open question which would deserve a dedicated investigation. It must be noted however that the production cross sections for t and ^{3}He particles measured in the same experiments were found almost identical [28].

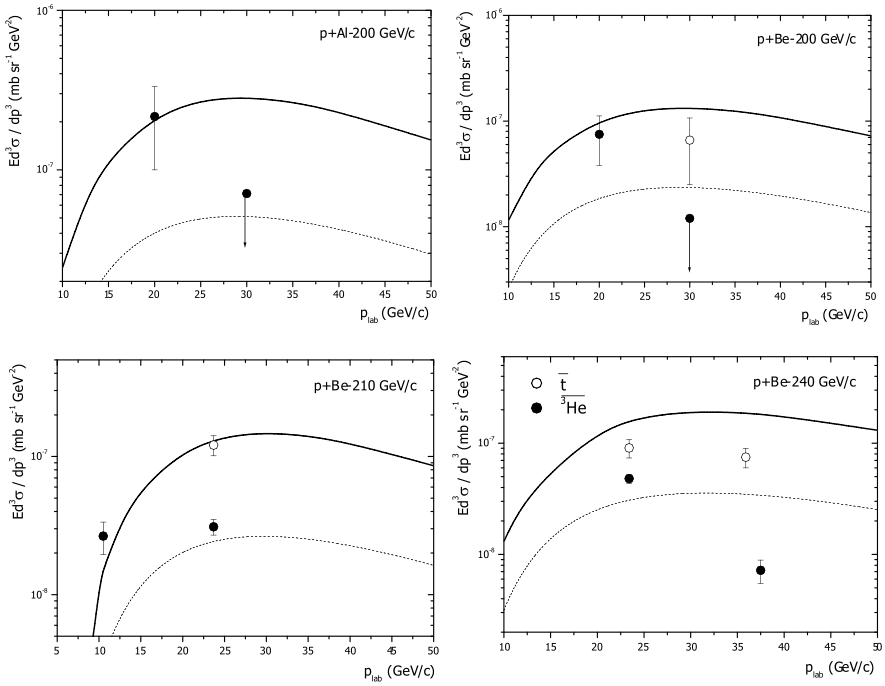

FIG. 4. Comparison of the production cross section for mass 3 antinuclei calculated by means of the standard (dashed line) and microscopic (solid line) coalescence model as described in the text.

III. OTHER CROSS SECTIONS REQUIRED FOR THE CALCULATIONS

A. Total antimatter reaction cross sections on nuclei

The total reaction cross sections $\sigma_R(\bar{a}A)$ for light antinuclei $\bar{a}$ collisions on nuclei A are needed for computation of the absorption term in the LBM or DM transport equations.

1. Antiprotons

For the galactic propagation, the $\sigma_R(\bar{p}p)$ total reaction cross sections for the $\bar{p}p$ collisions were calculated following [47], while for $\bar{p}^4\bar{\text{He}}$ collisions they were calculated from the former in the Glauber approximation as described in the next section (see [46] for more details).

For the atmospheric propagation of $\bar{p}s$, the total reaction σ_R and annihilation σ_{ann} cross sections for $\bar{p}A$ collisions on light nuclei (^{14}N and ^{16}O) were calculated using the following formulas (in mb):

$$\sigma_R = \left(257.8 + \frac{88.7}{T}\right)\left(\frac{A}{12}\right)^{2/3}, \tag{6}$$

$$\sigma_{\text{ann}} = 0.661(1 + 0.0036T^{-0.774} - 0.902T^{0.0151})A^{2/3}, \tag{7}$$

T being the particle kinetic energy. This relation is based on a similar formula given in [48] (p. 39 of this reference), with the $A^{2/3}$ dependence added. The resulting fit is shown in Fig. 5.

2. Antideuterons

A few experimental data for the total reaction cross section $\sigma_R(\bar{d}A)$ are available [49,50]. The same functional dependence on the nuclear mass number A as obtained in [49] has been used in this work:

$$\sigma_R = 105A^{2/3}mb. \tag{8}$$

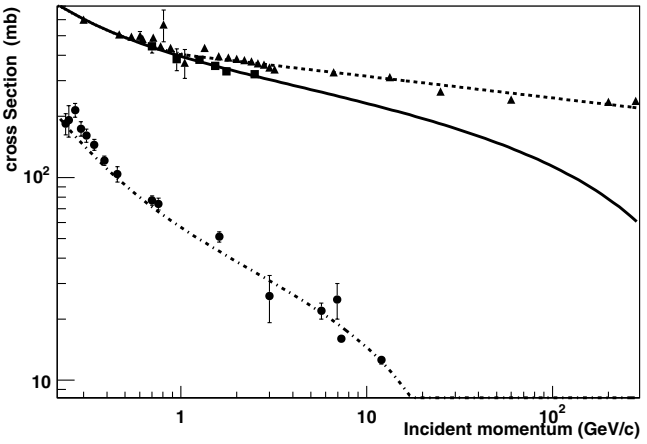

FIG. 5. Total $\bar{p}$ reaction cross section on the on ^{12}C (full triangles, see [48] for the sources of data), compared with the fit using relation (6) (dashed line). The $\bar{p}$C annihilation data (full squares) are compared with a fit using relation (7) (solid line). The $\bar{p}p$ annihilation data (full circles) are compared with the fit to the data points from [47] (dot-dashed curve).

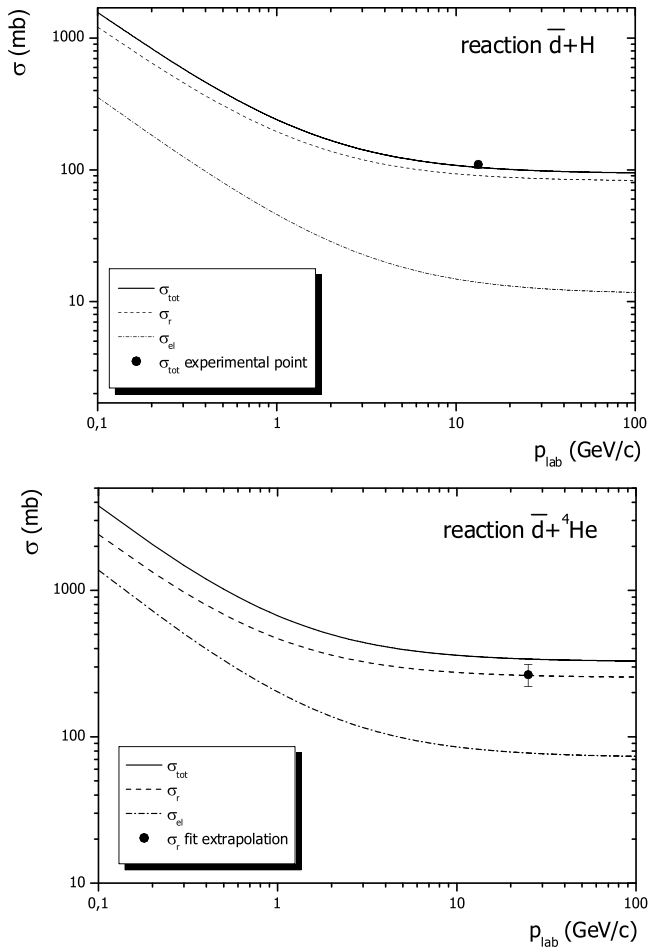

FIG. 6. Top: Total $\bar{d}p$ cross section data from [50] compared with the calculated values in the single scattering approximation of the Glauber model, as explained in the text. Note the good agreement between calculations and data. Bottom: Comparison of the total $\bar{d}^4$He reaction cross section obtained using the empirical relation (8) (full circle, the error bar is from [49]), with the Glauber approximation results (dashed line). The calculated total (full line) and elastic scattering (dash-dotted line) cross sections are also given, for completeness. See text for details.

The total reaction cross sections have also been calculated using the Glauber approximation and the parameters of the elementary $\bar{p}p$ scattering amplitude using the $\bar{N}N$ amplitudes from the analysis of [51]. The results are compared in Fig. 6 with the experimental results on the proton target and with the empirical parametrization from relation (8). See [46] for more details.

3. Mass 3 and 4 antinuclei

For the mass 3 and 4 antinuclei, the total reaction cross section has been calculated in the same eikonal approach as for the $\bar{p}A$ and $\bar{d}A$ systems, using the known matter distribution of the colliding nuclei and the nucleon-antinucleon amplitudes [46,51].

B. Nonannihilating inelastic rescattering

Before proceeding to the calculations of the propagated fluxes, the important issue of the rescattering of the transported particles is discussed in this section and more extensively in the appendix.

The low kinetic energy range—$T \lesssim 500$ MeV per nucleon—antideuteron flux is most sensitive to the possible primary $\bar{d}$ flux originating from exotic astrophysical sources such as primordial black holes [3] or dark matter (neutralinos) annihilation [2]. Any calculations of the secondary flux aiming at a good accuracy for low energy particles must then take into account all the significant effects contributing to populate this energy-momentum region. Note that this argument holds qualitatively as well for antiprotons or any other particle or antiparticle propagating in the interstellar medium. The rescattering of particles involves some energy loss and thus the transfer of a fraction of the flux from a given energy to a lower energy. The energy loss induced by the elastic scattering of the transported particles at the energies considered here involves only small momentum transfers. It is negligible. The inelastic process $\bar{d}p \rightarrow \bar{d}X$ may involve large energy-momentum loss of the scattered particles. A reliable description of the secondary flux in the low energy region should thus take into account the component induced by the $\bar{d}p \rightarrow \bar{d}X$ nonannihilating inelastic (re)scattering (NAR) reaction of the particles propagated in the ISM. This rescattering component will be referred to as tertiary in the following.

1. Principles

It has been argued recently that $\bar{d}$ (or symmetrically d) particles incident on a nucleon or on a nuclear target should have a small inelastic scattering cross section because of their natural ''fragility'' originating in the small $\bar{d}$ (d) nuclear binding energy, since a deuteron bound by only 2.2 MeV easily dissociates in a collision. This intuitive argument is misleading, however, and appears not to be correct after a careful examination of the problem. It can be invalidated both on empirical evidence and on formal grounds. The former consists of the existing experimental evidence of a deuteron [52,53]—and more generally nuclei [54]—induced nucleon excitation cross section (see also Sec. III B 2 below). The latter requires a few developments given in the appendix where it is shown on general grounds that the inelastic scattering cross section of light nuclear systems is in fact expected to be larger than the corresponding (p, p') or $(\bar{p}, \bar{p}')$ cross section, basically on the simple argument that it is driven by the NN $(\bar{N}\bar{N})$ elementary cross section folded with the matter distribution of the colliding systems. This is in agreement with the available experimental facts.

Effects of the isospin selection rules.—This picture is somewhat blurred however in the case of the inelastic (d, d') reaction on the nucleon since the inelasticity is strongly

inhibited at low incident energies by the isospin selection rule, the isovector excitations in the target nucleon being forbidden for this reaction. The deuteron is an isoscalar particle with isospin 0 which cannot induce isovector (i.e., with isospin quantum number $T = 1$) excitations in a nucleon (Δ resonances), in single step transitions. This has a strong inhibition effect on the total inelasticity of the reaction since the first excited state of the nucleon is the (isovector) $P_{33}\Delta$ resonance which in addition largely dominates the excited nucleon spectrum when the transition is permitted in inelastic processes like (e, e') or (p, p'). No direct nucleon excitation is thus permitted in (d, d') below the first (isoscalar) N^* resonance in hadron collisions, namely, below the 1.4 GeV (Roper) and 1.52 GeV [55] resonances in the nucleon.

The overall inelasticity is not totally hindered however since two step excitations via the nucleon (Δ) resonance(s) in the deuteron are allowed and have been observed experimentally [52,56].

2. Practical method

On account of the complex interplay between the underlying NN cross sections and selection rules which govern the $\bar{d}p$ inelastic cross section as discussed above, the practical approach used here has been based on empirical grounds. The energy integrated $\bar{d}p \rightarrow \bar{d}X$ cross section has been inferred from the experimental values of the cross section for the symmetric system $\bar{p}d \rightarrow Xd$ which should be identical at the same center of mass energy [50]. Figure 7 shows the experimental values for $\bar{p}d \rightarrow (n\pi)\bar{p}d$ (n multiplicity of produced pions) reactions as a function of the incident energy [57]. The total inelastic NAR cross section $\sigma_{\rm in}(\bar{p}d)$ has been obtained by summing up the $\bar{p}d \rightarrow (n\pi)\bar{p}d$ cross sections experimentally available, leading to $\sigma_{\rm in}(\bar{p}d) \approx 4mb$. No attempt was made to evaluate the (expectably small) contributions of the channels not known experimentally. The overall evaluation is thus quite conservative. Note that these data also support the arguments in favor of a non-negligible $\bar{d}(d)$ inelastic cross section, given in the previous section. For the momentum spectrum of inelastically scattered particles, the same functional form as in [58] was used to fit the data measured in these works, where the $pp \rightarrow pX$ inclusive cross section was found to be independent of the longitudinal momentum in the center of mass p_l^*, and could be described in the laboratory as

$$\frac{d^2\sigma(pp \rightarrow pX)}{dpd\Omega} = \frac{p_p^2}{2\pi p_t}\frac{\gamma(E - \beta p\cos\theta)}{E} 610 p_t^2 e^{-(p_t/0.166)} \tag{9}$$

where γ and β are the usual Lorentz factor and particle velocity and p_t the transverse momentum of the particle. The integrated cross section was normalized to the value determined as above for a given $\bar{d}$ incident energy.

The ansatz used in previous works for the energy distribution of the secondary particles was based on the limiting fragmentation hypothesis [59]. The form used for the energy dependence of the differential cross section $d\sigma(E, T_0)/dE \sim 1/T_0$ just corresponds to a constant differential cross section over the energy range of the produced particles between 0 and the incident kinetic energy T_0 in the laboratory frame. Experimentally, the $pp \rightarrow pX$ differential cross section was shown to be largely independent of the longitudinal momentum p_l^* of the produced particles in the center of mass [58] (see also [34]). Figure 8 shows the inelastic scattering spectra in the laboratory for 2 and 3 GeV incident kinetic energy protons obtained in the approximation of [59] (flat spectra) and used in this work, after [58]. The effects of the observed differences on the galactic flux of particles are discussed in Sec. IV B 2 below.

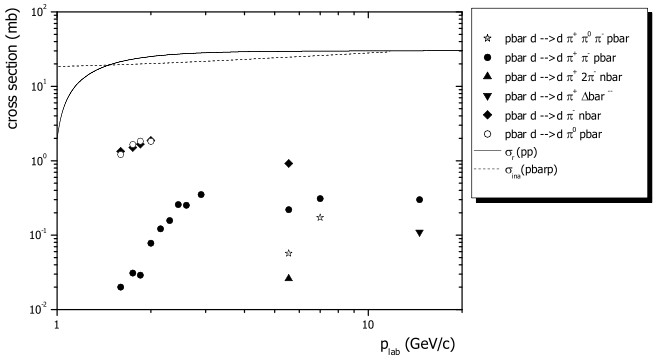

FIG. 7. Partial $\bar{p}d \rightarrow (n|\pi)\bar{p}d$ cross sections from [57] used to evaluate the total inelastic NAR $\bar{d}p \rightarrow \bar{d}X$ cross section.

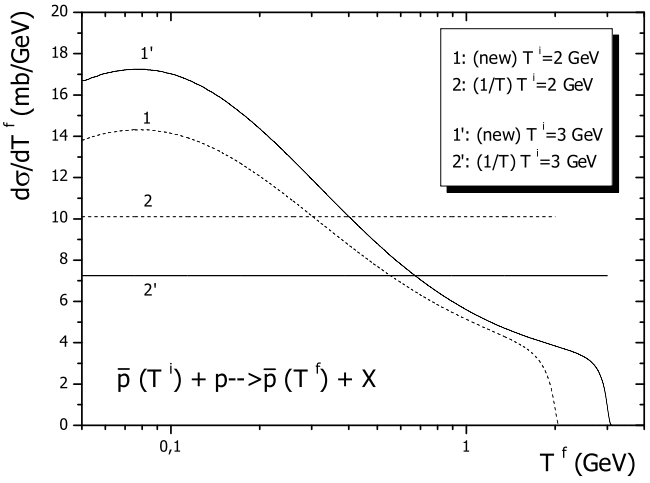

FIG. 8. Spectral distributions of inelastically scattered protons (antiprotons) from a hydrogen target in the approach of [59] (horizontal lines) and used in this work for evaluating the NAR contributions of the antinuclei flux, for 2 GeV (dashed lines) and 3 GeV (solid lines) incident kinetic energies.

IV. GALACTIC ANTIMATTER PRODUCTION AND PROPAGATION

In the previous sections, the hadronic and nuclear physics issues related to light antinuclei production and interactions have been reviewed and updated. The present section addresses now the flux propagation of the produced antimatter nuclei in the framework of the leaky box model. The model is simple, widely successful, and highly useful, with a sound predictive power for use with purposes such as the present one. It rests on a single effective phenomenological parameter—the escape length $\lambda_{\rm esc}$ [60]—incorporating the physics (diffusion and convection) of the transport process. The leaky box model avoids lengthy discussions about what should be the value of the galactic transport parameters in more realistic models. It is an economical way to obtain reliable results. As such, it is very well suited to address the impact of the cross sections obtained here and in [14] on the $\bar{p}$ and $\bar{d}$ fluxes.

The errors on the $^3\bar{\rm He}$, $^4\bar{\rm He}$ and to a lesser extent, $\bar{d}$ production, are the dominant source of uncertainty. Even for $\bar{p}s$, the inaccuracy on the production cross section has been estimated to be larger than that related to the propagation parameters in [1]. For heavier antinuclei $\bar{A}$, the production rate is proportional to $p_0^{\bar{A}-1}$. An uncertainty of Δp_0 on the coalescence parameter leading to an uncertainty $\Delta\Phi_{\bar{d}}$ on the antideuteron flux translates into an uncertainty $(\bar{A}-1)\Delta\Phi_{\bar{d}}$ for these antinuclei.

The following subsections compare in details the $\bar{p}$ and $\bar{d}$ fluxes with previous results for the various contributions from nuclear reactions, diffusive reacceleration, and solar modulation. The results derived in the simple LBM are then compared to more realistic calculations performed in the DM framework. The section also includes the presentation of $^3\bar{\rm He}$ and $^4\bar{\rm He}$ fluxes and ends with a summary of the calculated fluxes.

A. The leaky box model for cosmic ray propagation

In this model, the flux $\Phi_{\bar{A}}(T_{\bar{A}})$ of the antinucleus $\bar{A}$ at kinetic energy $T_{\bar{A}}$ is given by

$$\Phi_{\bar{A}}(T_{\bar{A}}) = \frac{\lambda_{\rm esc}(T_{\bar{A}})\lambda_{\rm int}(T_{\bar{A}})}{\varrho_{\rm ISM}[\lambda_{\rm esc}(T_{\bar{A}}) + \lambda_{\rm int}(T_{\bar{A}})]} \times \frac{1}{4\pi}[Q^{\rm sec}_{\bar{A}}(T_{\bar{A}}) + Q^{\rm ter}_{\bar{A}}(T_{\bar{A}})] \qquad (10)$$

with $Q^{\rm sec}_{\bar{A}}(T_{\bar{A}})$ and $Q^{\rm ter}_{\bar{A}}(T_{\bar{A}})$ being the secondary and tertiary source terms discussed below, respectively, and where $\lambda_{\rm int}(T_{\bar{A}}) = \langle m\rangle/\langle\sigma_R^{\bar{A}+{\rm ISM}}(T_{\bar{A}})\rangle$ and $\lambda_{\rm esc}(T_{\bar{A}})$ are taken from [61]. Following [62], we use the quantities $\langle m\rangle = 2.05\times10^{-24}$ g for the average mass of the interstellar gas, $\varrho_{\rm ISM} = 2.28\times10^{-24}$ g cm^{-3} for the ISM average density, and $\langle\sigma_R^{\bar{A}+{\rm ISM}}(T_{\bar{A}})\rangle$ stands for the average reaction cross section on this gas. The ISM composition used is H:He:C:N:O = 1:0.1:5×10^{-4}:8×10^{-4}:8×10^{-5} cm^{-3}. Actually, these numbers as well as the average density are not perfectly known. The requirement to fit the B/C ratio for a given choice for these quantities leads to a peculiar parametrization for $\lambda_{\rm esc}(T_{\bar{A}})$. However, a different choice than the above, if it would probably affect the normalization of the fluxes, would have a minor effect on the shape of the distribution. It is thus sufficient to check that the choice made for $\langle m\rangle$, $\varrho_{\rm ISM}$, and $\lambda_{\rm esc}$ leads to the correct normalization of the spectra. Tested on the $\bar{p}$ spectrum, the same set of parameters can then be safely applied to the other antinuclei fluxes.

Concerning the secondary $Q^{\rm sec}_{\bar{A}}$ and tertiary $Q^{\rm ter}_{\bar{A}}$ source terms in relation (10) above, the former results from the net creation of the antinucleus $\bar{A}$ from CR interaction on the ISM (see Sec. II), whereas the latter results from the energy redistribution through inelastic nonannihilating (NAR) reactions of the produced antinuclei, discussed in detail in Sec. III B above. Note that neither the ionization losses nor the reacceleration process were included in the LBM calculations. They were, however, taken into account in the DM results presented in Sec. IV B 3. The main new features of the present calculations with respect to previous works are the following:

(1) The antinuclei production cross sections used are more tightly constrained by the available data [14].
(2) The standard coalescence model for the production cross section of composite particles has been calibrated and validated on the available inclusive production cross section of light antinuclei ($\bar{d}$, $\bar{t}$, $^3\bar{\rm He}$), and an independent microscopic (diagrammatic) coalescence approach was also used.
(3) The inelastic rescattering of the transported particles are taken into account in a more realistic way than in previous works.
(4) The contribution of the $\bar{p}p \to \bar{d}X$ reaction cross section was included in the calculated $\bar{d}$ flux.

B. Antiprotons and antideuterons

For the $\bar{p}$ flux, the two source terms are

$$Q^{\rm sec}(T_{\bar{p}}) = 2\sum_{\rm i=CRs}^{\rm p,He,CNO}\sum_{\rm j=ISM}^{\rm H,He,CNO} 4\pi n_j \int_{6m_p}^{\infty}\frac{d\sigma^{\rm i+j}}{dT_{\bar{p}}} \times (T_{\bar{p}}, T_i)\Phi_i(T_i)dT_i, \qquad (11)$$

$$Q^{\rm ter}(T_{\bar{p}}) = 4\pi.n_p\Big[2\int_{T_{\bar{p}}}^{\infty}\frac{d\sigma^{\bar{p}p\to\bar{p}X}}{dT_{\bar{p}}}(T'_{\bar{p}}, T_{\bar{p}})\Phi_{\bar{p}}(T'_{\bar{p}})dT'_{\bar{p}} - 2\sigma^{\bar{p}p\to\bar{p}X}_{\rm NAR}(T_{\bar{p}})\Phi_{\bar{p}}(T_{\bar{p}})\Big], \qquad (12)$$

where n_p is the hydrogen number density in the ISM in cm^{-3}, $d\sigma^{\rm i+j}/dT_{\bar{p}}$ is the differential $\bar{p}$ production cross section, $d\sigma^{\bar{p}p\to\bar{p}X}/dT_{\bar{p}}$ is the differential inelastic nonannihilating cross section for $\bar{p}s$ with incident energy $T'_{\bar{p}}$ emerging from the collision with an energy $T_{\bar{p}} < T'_{\bar{p}}$, and

$\sigma_{\rm NAR}^{\bar{p}p\to\bar{p}X}$ is the total inelastic scattering $\bar{p}p \to \bar{p}X$ cross section. This latter term involves the quantity $\Phi_{\bar{p}}(T_{\bar{p}})$ in the integrand, requiring a numerical method to be used to solve Eq. (10). Following [1], the tertiary contribution on He is taken into account assuming a mere scaling factor $4^{2/3}$ to the corresponding cross section on hydrogen. The factor of 2 in front of both terms in (11) takes into account the $\bar{n}$ (decaying into $\bar{p}$) production cross section, assuming the $\bar{p}$ and $\bar{n}$ production cross sections are the same.

For antideuterons, the source terms are similar (with $\bar{p}$ labels changed to $\bar{d}$) with only the pp, pHe, and Hep incoming channels for the production reaction (threshold $16m_p$ for the pp incoming channel) taken into account (heavier components neglected). The new contribution $Q^{\rm ter}$ ($\bar{p}p$ and $\bar{p}$He, threshold $6m_p$), which was assumed to be negligible in [2], was included here. In $Q^{\rm sec}(T_{\bar{d}})$ the term $d\sigma^{\rm CRs+ISM}/dT_{\bar{d}}$ was evaluated by means of the coalescence models discussed in Sec. II A.

Note that for the primary fluxes of p and He, the parametrization provided by the AMS01 experiment was used. Since the flux measurements of the BESS [9] and AMS01 [5] experiments are now compatible, the primary fluxes can then be considered as being a minor source of uncertainty of the calculations [1].

1. The secondary source term

Figure 9 shows the various contributions to the source term $Q^{\rm sec}(T_{\bar{p}})$ as defined in relation (12) (independent of any propagation model) for the antiproton (upper panel) and antideuteron (lower panel) fluxes.

For the antiproton flux, the pp reaction contributes about 56% to the $\bar{p}$ production, the pHe up to 24%, the Hep up to 12%, and the HeHe reaction up to 6%. The latter has been evaluated by scaling the $pp \to \bar{p}X$ cross section using the same procedure as described in [63]. The reactions $p-$CNO and CNO $-p$ contribute to less than 2%, while He $-$ CNO and CNO $-$ He have been neglected in account of the very low CNO nuclei flux and IS density. These components are compared in the figure to those obtained in [1,62] using the cross sections calculated using the DTUNUC event generator. At the production peak, for pp and pHe reactions, the calculated yields are similar up to 10%. There is a trend of the present calculations to predict smaller cross sections than DTUNUC for particle energies above a few GeV. In the low energy range $T_{\rm kin} \lesssim 1$ GeV, it is seen in the figure that DTUNUC clearly predicts a larger [62] or even much larger [1] target compositeness effect than in the present work, with a larger low energy cross section calculated for composite targets ($A \geq 4$) than for the proton target. This difference would deserve a further investigation both theoretical and experimental, of the low energy $\bar{p}$ yield in nuclear collisions. Note however that for the pp induced yield, the present calculations predict a larger flux at very low energies than the DTUNUC based calculations. It must also be remembered that this energy range is marginally within the DTUNUC domain of validity.

For the antideuterons (lower panel), the contributions from the pp, pHe, and Hep collisions are peaked around 4 GeV/n and the obtained distributions display a similar bell shape as obtained for the IS $\bar{p}$ flux. This feature can be easily explained qualitatively since the calculated distributions of the $\bar{d}$ ($\bar{p}$) fluxes are driven on the low energy side

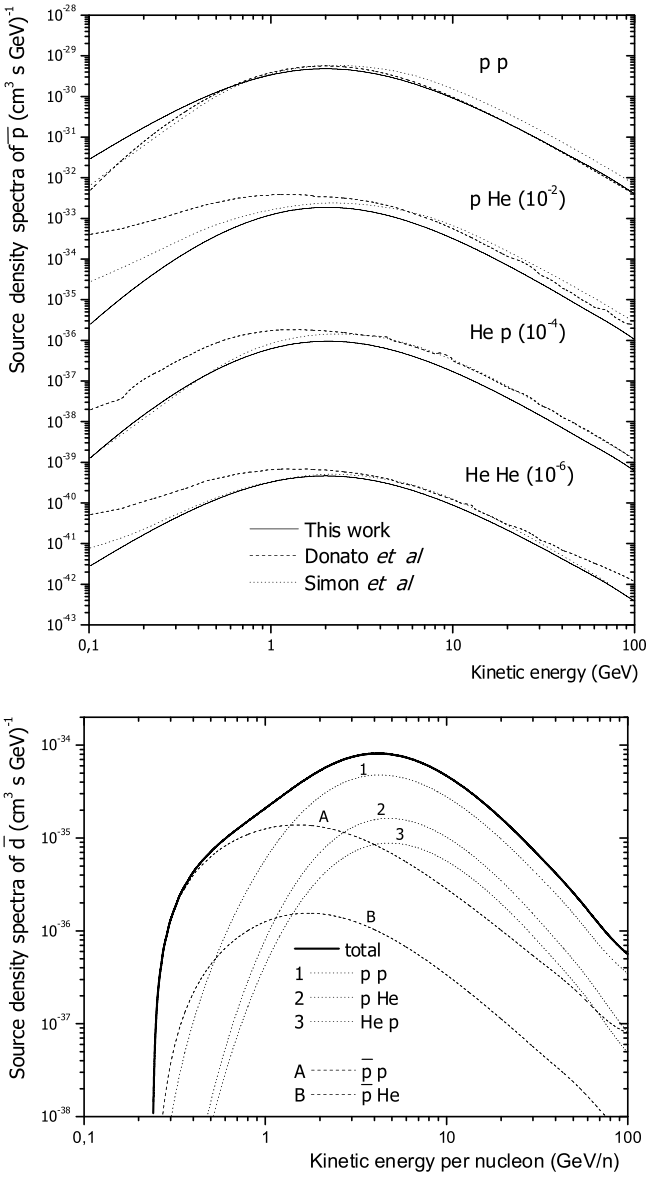

FIG. 9. Source terms for antiproton and antideuteron particles as defined in relation (11). Upper panel: $Q^{\rm sec}$ for the antiproton production from the present work (solid lines), compared with the results from two different papers using the DTUNUC event generator ([1]: dashed lines; and [62]: dotted lines). Note that the curves taken from [62] (dotted lines) correspond to slightly different H and He input fluxes compared with the two other models presented. Lower panel: $Q^{\rm sec}$ for the antideuteron production for the different channels considered in this work. See text for details.

by the rapidly rising $\bar{d}$ ($\bar{p}$) production cross section with energy above the $\bar{d}$ ($\bar{p}$) production threshold (see [64], for example), while the high energy decay of the distribution is determined by the rapidly decreasing incident CR proton flux with energy, folded with the natural decrease of the high energy production cross section (see Fig. 3).

These dynamical and kinematical characteristics (see Sec. II C 2) are responsible for the $\bar{p}p \rightarrow \bar{d}X$ contribution to the flux to be clearly dominant over the entire low energy range below 1 GeV/n with a value larger than the value reported in [2,20] by about 1 order of magnitude (note that the $\bar{p}^4\mathrm{He} \rightarrow \bar{d}X$ contribution can be neglected here, as it can be seen by comparing curve A to curve B in Fig. 9). At energies above 2 GeV, this flux becomes rapidly negligible.

Note that for this channel, the $\bar{p}$ flux was calculated conservatively using the parametrization providing the smaller values for the cross section. The range of integration for the $\bar{d}$ flux calculation has been limited to 100 GeV $\bar{p}$ incident energy (while for $pp \rightarrow \bar{p} + X$, the integration was performed up to a few tens of TeV p energy to calculate the $\bar{p}$ production), since the $\bar{p}$ flux beyond 100 GeV is vanishingly small. The major source of error here is due to the uncertainty on $\bar{p}$ flux in the few GeV range. For example, a roughly twice larger $\bar{d}$ flux could be produced in this channel by taking the mean values of the experimental data points for this flux, rather than the $\bar{p}$ flux obtained from the $\bar{p}$ data fits. For the other channels, the uncertainties are related to those for the $\bar{p}$ production, combined with the contribution induced by the coalescence model. It must be emphasized however that, although the procedure used to evaluate this cross section is based on the underlying physics, the error induced by the approximations made in this approach cannot be accurately evaluated.

In conclusion of this section, it has been shown that the secondary $\bar{p}p \rightarrow \bar{d}X$ term does contribute significantly to the IS galactic $\bar{d}$ flux, and that it is even dominant in the low kinetic energy $T_{\bar{d}} \lesssim 1.5$ GeV/nucleon range.

2. The tertiary source term

The only tertiaries considered here are those created by the nonannihilating inelastic scattering of secondaries on the ISM (NAR process). This contribution was first included for $\bar{p}s$ in [65].

The sharp kink observed in the low energy $\bar{d}$ spectrum in the lower panel of Fig. 10 can be better understood by examining how inelastically scattered antiprotons or antideuterons are redistributed, since the redistribution mechanism may have significantly different effects on the respective shapes and intensities for the $\bar{p}$ and $\bar{d}$ flux. Since the Q^{ter} term in Eq. (12) has to be integrated numerically, the same iterative procedure as proposed in [1] was used. For antiprotons, a few iterations are required, while only one single iteration is needed for antideuterons. This is simply due to the much larger relative inelastic (NAR) cross section compared to the total cross section for $\bar{p}p$ than for $\bar{d}p$ collisions (see Sec. III B and appendix), which makes the numerical convergence slower in the former case. To better understand the details of the transfer process to lower energy, the tertiary contributions from three kinetic energy bands ($\mathrm{T} < 2$ GeV, $2 < \mathrm{T} < 10$ GeV, $10 < \mathrm{T} < 100$ GeV) are displayed separately in Fig. 10. The corresponding curves were obtained by first evaluating the equilibrium spectrum, and then computing from this spectrum the tertiary yield from the chosen energy bands.

For the antiprotons (Fig. 10, upper panel), the NAR cross section is large and the low energy tail is largely replenished. Several iterations are required to obtain the equilibrium flux allowing the second order NAR contribution to be significant, the first iteration replenishing both the medium and low energy bands, the former of those replenishing the low energies in the next iteration step.

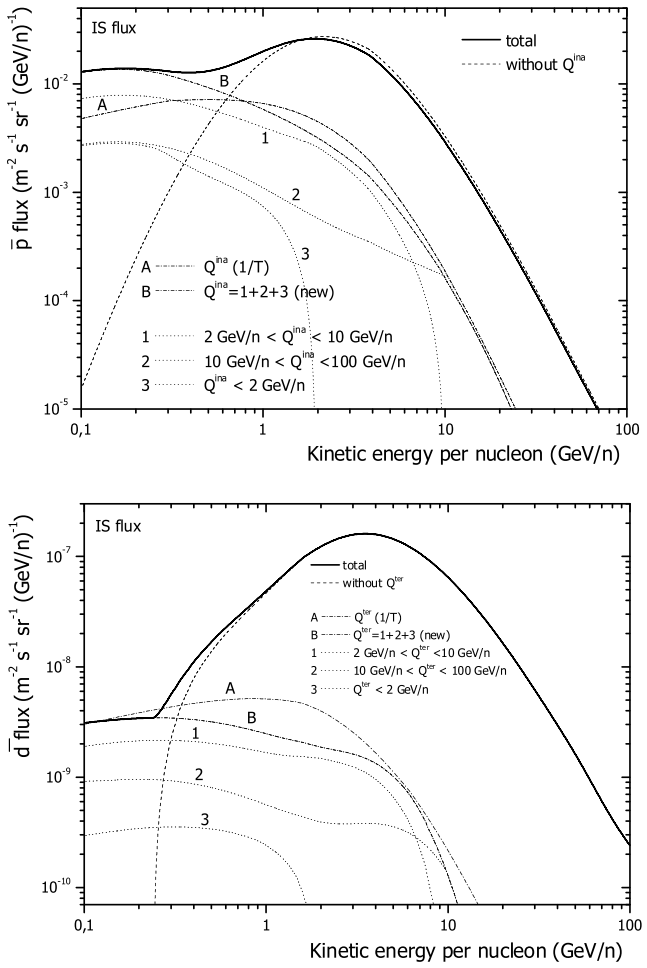

FIG. 10. Comparison of tertiary contribution using the standard $1/T$ parametrization (A) and the parametrization used in this work (B) for the $\bar{p}$ (upper) and $\bar{d}$ (lower) fluxes. The B tertiary component is further decomposed into individual contributions from three energy bands (labels 1, 2, and 3). See text for details.

For the antideuterons, the NAR cross section is much smaller than for $\bar{p}s$. The first consequence is that the tertiary component is almost 2 orders of magnitude smaller than the peak value of the secondary component (while it is less than 1 order of magnitude smaller for $\bar{p}s$). One single iteration is thus required in the process and the contribution of second order interactions is negligible. This explains the sharp upturn in the $\bar{d}$ flux that is not seen in the $\bar{p}$ spectrum. The secondary flux drops rapidly at low energy and the tertiary and secondary components become comparable only at ≈ 300 MeV/n. In this case the NAR process does not accumulate particles at low energies as efficiently as in the antiproton case because of the much smaller NAR cross section (compare the two curves labeled 3 in the upper and lower panels).

The effects of the NAR spectrum on the $\bar{p}$ and $\bar{d}$ distributions are also illustrated in the figure, with the curves labeled A and B corresponding to the parametrization used in [59] and here (see Sec. III B 2), respectively. Although for $\bar{d}s$ the results are hardly different at the lowest energies, for $\bar{p}s$ the more realistic inelastic spectrum leads to a low energy NAR flux larger by almost a factor of 2 than the other option.

3. Discussion of the interstellar fluxes

a. Comparison to previous published fluxes

The upper panel of Fig. 11 shows the results from the present work for the unmodulated antiproton fluxes compared with some previously published results. For the present calculations (full lines), the two curves correspond to the two different parametrizations used for the $\bar{p}$ production reaction in pp collisions [14]. The present results are close to those from [66] (dashed line). Both rely on better fits to the data than in [47]. The latter, used in the present approach, would give a flux standing roughly midway between the two full lines for $\bar{p}$ energies above 1 GeV. The so defined range can thus be considered as the uncertainty due to the production cross section.

In the results of the diffusion model [1], the flux is somewhat higher at high energy, while at low energy the effect of reacceleration is responsible for the much larger predicted flux (note the enlarged vertical scale in Fig. 11). However, it will be seen below that the two results are not so different after modulation. Note that as the parameters used for the present calculations provide the correct magnitude for the calculated fluxes (see upper panel of Fig. 14), they can be used confidently to evaluate the galactic fluxes for other antinuclei.

The lower panel of Fig. 11 shows the calculated antideuteron flux (dotted line) evaluated as in Ref. [2] (dashed line), i.e., including neither the tertiary term (NAR) nor the $\bar{p}p$ included and using a coalescence parameter $p_0 = 58$ MeV. Note that the p and He galactic fluxes used in [2] were slightly different however from the more recent measurements used here. Note also that in [2], a diffusion model without reacceleration was used. The two calculations appear to be compatible. At low energy, the difference observed in the antideuteron flux from the two approaches originates from the following:

(1) The difference between the low energy $\bar{p}$ production cross section used here and that from [47] (dominant effect).

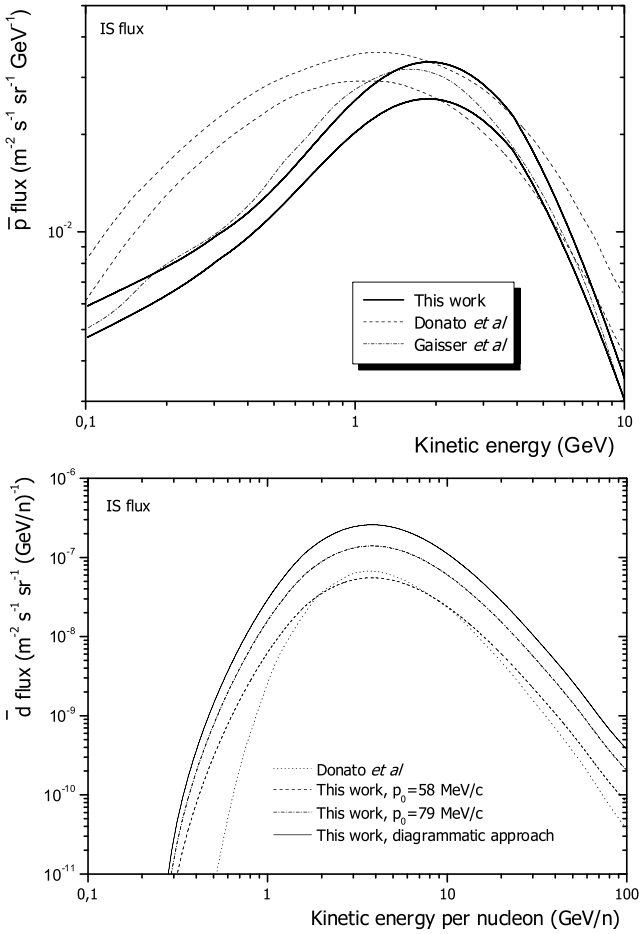

FIG. 11. Partial calculations of galactic antiproton (upper panel) and antideuteron (lower panel) interstellar fluxes for comparison purpose. Upper panel: The present calculations (solid lines) are compared with those from [1] (diffusion model with reacceleration, dashed lines) and from [66] (leaky box model, dash-dotted line). The two curves from the present work (using standard NAR), obtained for the two different parametrizations of the production cross section, as well as those from [1], indicate the level of uncertainty of the results due to hadronic cross sections. Lower panel (no tertiaries): Present results (pp, pHe, and Hep contributions only) using the standard coalescence model (fitted to the $\bar{d}$ data) with $p_0 = 79$ MeV (dash-dotted line) and the diagrammatic approach of coalescence (solid curve). The two lower curves show the present calculations using the same coalescence parameter $p_0 = 58$ MeV (dashed line) as in [2] (diffusion model, no reacceleration, dotted line). See text for details.

(2) The kinematics of the $\bar{p}$ production near the threshold, also modeled differently here than in [1], providing a larger antiproton—and thus antideuteron—cross section, over this range.

The upper two curves (solid lines) in the figure, correspond to the standard model (reference calculation, lower curve) and to the microscopic model calculations discussed in Sec. II C (upper curve).

b. Full calculation

Figure 12 displays the full calculation results for the IS fluxes obtained in this work. The upper panel shows the two calculations showing the uncertainty on the pp production channel induced by the two parametrizations used [dedicated pp (II), and pA with $A = 1$ (I); see Sec. II B and [14]].

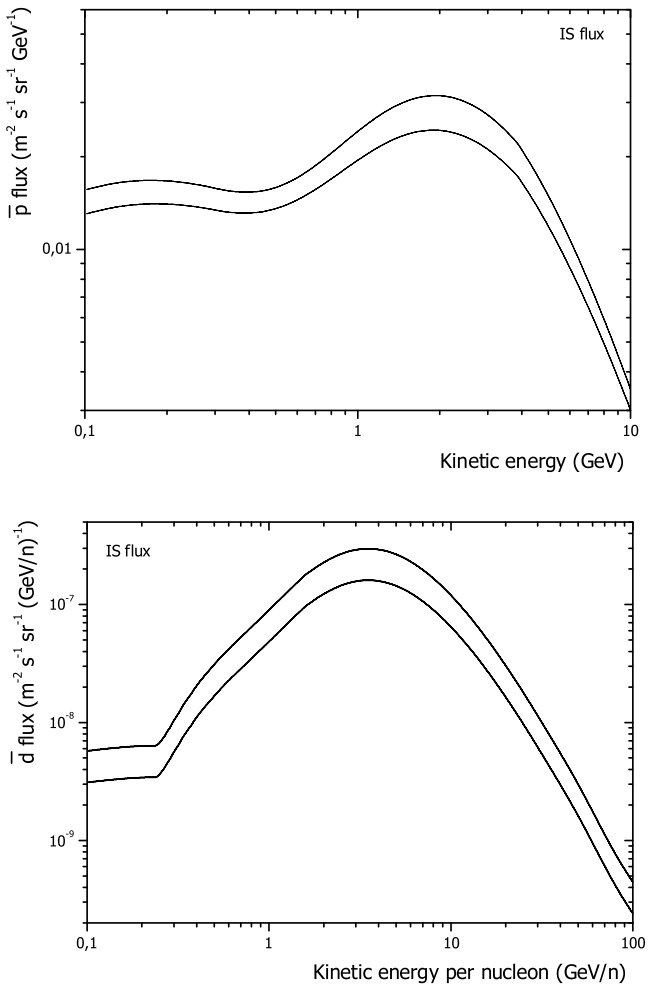

FIG. 12. Upper panel: IS $\bar{p}$ flux including all contributions, the two lines showing the uncertainty due to nuclear cross sections (see text). Lower panel: $\bar{d}$ flux for the standard coalescence model (reference calculation, lower curve) and for the microscopic coalescence model.

It was seen in Secs. II C and IV B 1 that the uncertainty for the other channels that contribute to almost half of the flux is similar, their contributions having been evaluated using widely proven calculation methods based on existing experimental data. Comparing with the results obtained using the DTUNUC generator, large differences have been found for the various individual channel contributions, although a rough agreement for the overall secondary production has been obtained.

For the antideuteron flux (Fig. 12, lower panel), the lower curve shows the reference results obtained with the standard coalescence model (based on a fit of $\bar{d}$ data) and including all the secondary and tertiary components discussed previously. The overall uncertainty associated with the reference calculation is of the same order of magnitude as for the $\bar{p}$ flux, plus the coalescence model contribution to be added (see Sec. II C). It is estimated to be better than a factor of 2. The upper curve on the figure shows the microscopic coalescence model calculation (which overestimates the experimental data on the average).

At low energy, the $\bar{p}p \rightarrow \bar{d}X$ reaction can be estimated to be correct to within a factor of 2 regarding the accuracy of the inclusive $\bar{p}$ available data. The tertiary term corresponds to a pretty conservative lower limit since, based on the evaluation method used (see Sec. III B 2), the upper limit is less than a factor of 2. From this point of view, some direct measurements of the $\bar{p}p \rightarrow \bar{d}X$ production reaction would be extremely useful to eliminate the uncertainties corresponding to the approximations made here.

c. Comparison with the diffusion model

Figure 13 shows the diffusion model calculations for the $\bar{d}$ flux, with the same common inputs as in the present calculations, i.e., same p and He galactic flux and hadronic cross sections, including the $\bar{p}p \rightarrow \bar{d}X$ contribution. The top panel shows the results without diffusive reacceleration for the DM calculations. The agreement between the two results is good, except in the 500 MeV/n range where the $\bar{p}p \rightarrow \bar{d}X$ contribution is more salient in the present calculations than in the DM approach, making the predicted flux larger by a factor of about 2. The middle panel shows the DM calculations including the diffusive reacceleration term compared with the same present results as above. The observed effect of the reacceleration on the spectrum is similar to the effect of the solar modulation (compare with curve 1 in Fig. 14, lower panel), making the distribution at low energies below 1 GeV/n power-law shaped. The bottom panel shows the effects of the combined reacceleration term and solar modulation for the DM model, compared with the present calculation including the solar modulation effects. In this case, the general shape of the results are similar, the very low energy flux predicted to be larger from the DM calculations than from the present LBM by a factor of 2 to 4.

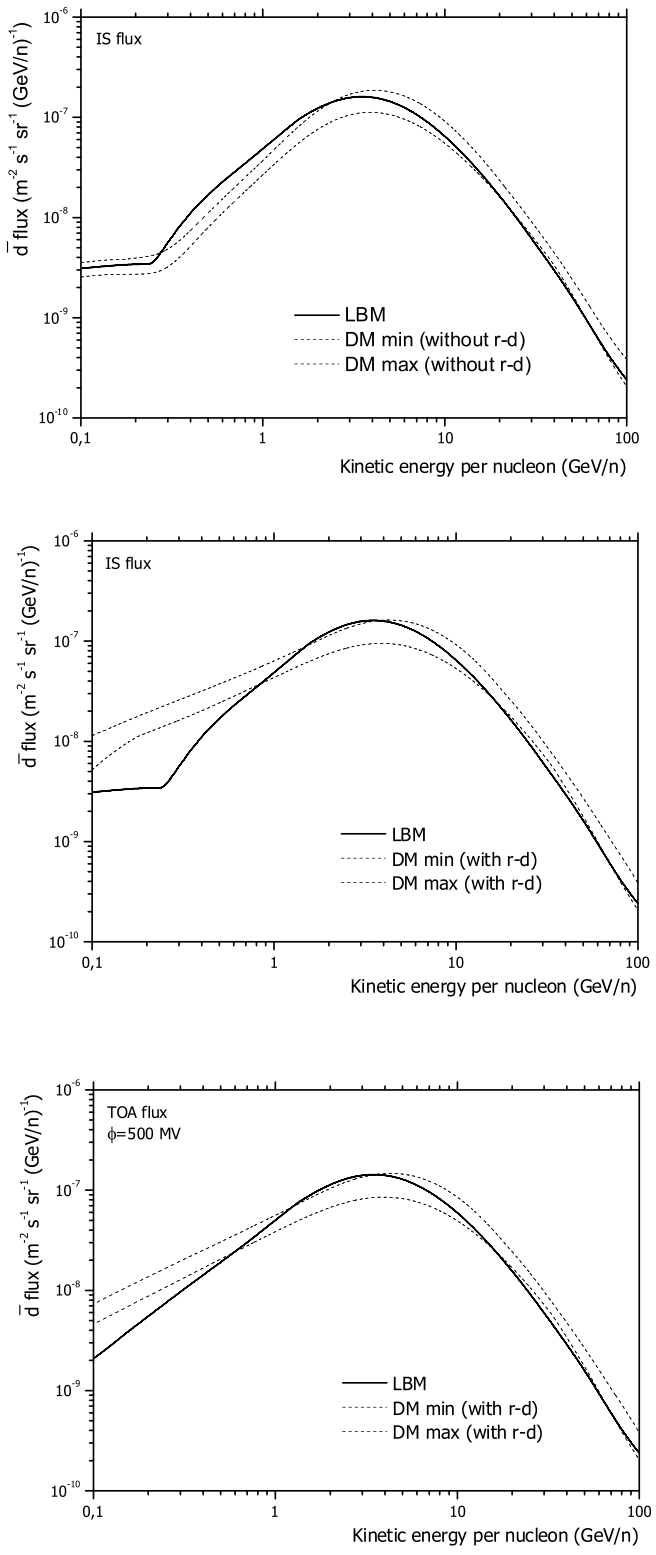

FIG. 13. Comparison of the present IS (unmodulated) $\bar{d}$ flux calculations (solid line) with the diffusion model results (dashed line), without (top) and with (middle) the reacceleration term included (see [21]), and with modulation and reacceleration included (bottom). The two lines for the DM results on the three panels correspond to the same estimated range of propagation uncertainty as evaluated in [21] and used for $\bar{p}$ in [1].

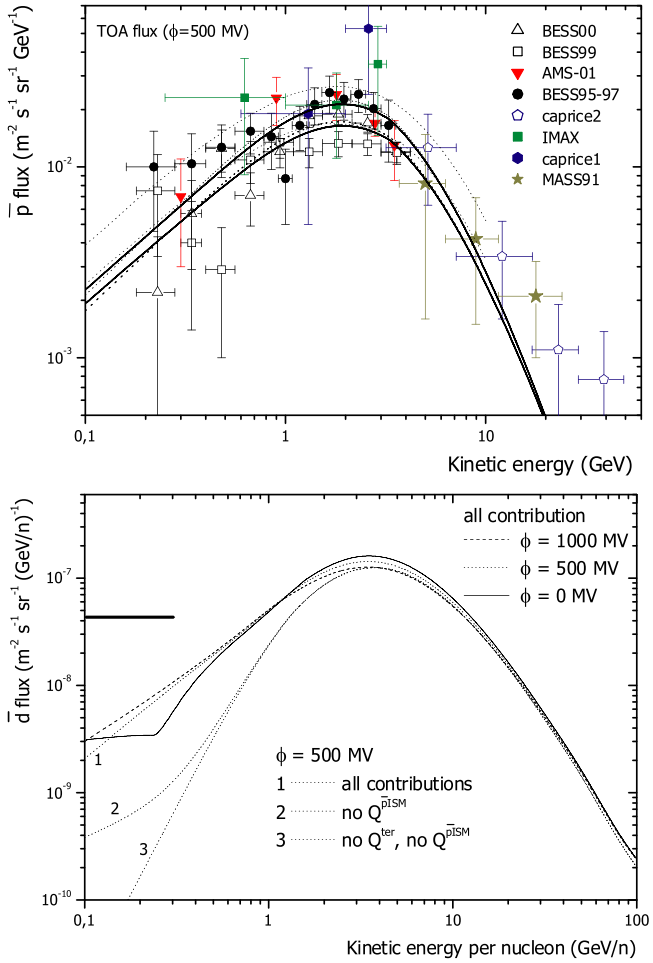

FIG. 14 (color online). Modulated antiproton fluxes. Upper panel: Present calculations, with the two line types corresponding to the single $pp \rightarrow \bar{p}X$ reaction, without (solid lines) and with (dashed lines) the NAR contribution. They are compared to the DTUNUC calculations (dotted lines), the two curves for the latter giving the overall production uncertainties as evaluated in [1] (see text for details). Note that the differences due to reacceleration, observed in the IS fluxes, are completely smoothened by the solar modulation effects. Lower panel: Same calculations with the curves labeled 1–3 giving the fluxes obtained, for the full calculation (label 1), with the contribution of the new ingredients $Q^{\bar{p}\mathrm{ISM}}$ switched off (label 2), and with both $Q^{\bar{p}\mathrm{ISM}}$ and the NAR Q^{ter} contribution switched off (label 3), for the same modulation level ($\phi = 500$ MV). The (typical) level of primary fluxes evaluated by various authors is shown by the thick solid straight line on the left [2,46] (see text).

4. Solar modulation effects

It has been seen in the previous sections that quite significant differences between the antimatter fluxes are predicted in the astrophysically sensitive low energy range of the studied particles. In this section, the solar modulation effects on the calculated flux are incorporated and their influence on the various components of the calculations together with the resulting overall accuracy are discussed.

The situation for the low energy spectrum is drastically different for the modulated fluxes, i.e. at TOA, than it was before for the IS spectra. The upper panel of Fig. 14 shows the antiprotons flux using the standard, i.e. flat spectrum, NAR cross section (solid lines) and the parametrization [58] used here (dashed lines) for a solar modulation parameter $\phi = 500$ MV. Whereas these two calculations produced very different IS fluxes (see upper panel of Fig. 10), they are hardly different once modulated. This is not surprising since the effects of the solar modulation are well known to occult the low energy range of the IS spectrum. This effect results in the present calculation improving the agreement (up to a sound normalization factor, however) with the results of the diffusion model with reacceleration (dotted lines) from [1]. For each case the two bands correspond as before to the uncertainties associated with the hadronic cross sections involved: for the present calculations (solid lines) they include (a) for the pp incoming channel, the uncertainties related to the I and II parametrizations; (b) for pA ($A > 1$) systems, the uncertainties of the fit to the data as quoted above (see [14]); (c) for AA ($A > 1$) systems, those related to the (Glauber) calculation procedure and its ingredients [46]. In [1] the uncertainty band was evaluated from the DTUNUC uncertainties with all the contributions of the relevant AA collision systems considered, combined together.

The $\bar{d}$ flux naturally suffers the same source of uncertainty due to the hadronic cross sections as for the $\bar{p}$ flux. The lower panel of Figure 14 illustrates the status of the various components of the $\bar{d}$ flux. The three curves labeled 1, 2 ,and 3 show the relative contribution of the various source terms for the same modulation parameter $\phi =$ 500 MV. As could be expected from Fig. 9, the $\bar{p}$ induced $\bar{d}$ production ($Q^{\bar{p}\mathrm{ISM}}$) dominates over the $\bar{d}$ rescattering (NAR) contribution (Q^{ter}) at energies smaller than about 500 MeV/n, where the latter is clearly negligible. This is even more true at a higher modulation level (compare the solid line, dotted line 1, and dashed line).

Finally, the thick solid horizontal line in the figure shows a lower limit for the estimates of primary source—supersymmetric particles annihilation (SUSY) or PBH evaporation—contributions in which fluxes in both cases drop rapidly to negligibly small values above 1 GeV/n. Some of these predictions [2,3] give fluxes that could be 1 order of magnitude larger than the quoted limit. Hence, this confirms that the antideuteron signal is probably a good tracer to look for SUSY, likely better than antiprotons, provided that $\bar{d}s$ can be discriminated from $\bar{p}s$ and electrons at the appropriate level of selectivity, i.e., with a rejection power of the order of 10^5, in the forthcoming experiments, which is quite an instrumental challenge.

5. Uncertainties on the calculated fluxes

In summary, in the context of using the $\bar{p}$ flux to derive constraints on new (astro)physics (primary exotic component), it can be considered that the NAR cross section is now evaluated with an improved accuracy, even if this accuracy is clearly not a major issue here since it has been seen that for rigidity $R \lesssim 0.5$ GV of the IS flux, all differences are swept away by the solar modulation effects. On the other hand, it must be emphasized that the significant differences observed between the results obtained from data fits, and used here for the production cross sections, and those obtained from the DTUNUC predictions (for AA collision systems), would certainly deserve a more complete investigation since they are a major source of uncertainty for the flux calculations.

Below 0.5–1 GeV/n, the contribution of the $\bar{p}p$ induced $\bar{d}$ flux which suffers many flaws as emphasized in Sec. IV B 1 is probably large. Within and below this region of energy, several sources of large uncertainties due to, in decreasing order of magnitude, hadronic cross sections, solar modulation, and propagation have been found to exist. These would dramatically increase the difficulty of reliable precision astrophysics measurements over this energy range. Above 1 GeV/n, the dominant source of uncertainties remains the hadronic cross sections.

C. Mass 3 and 4 antinuclei fluxes

The same calculations have been performed for the propagated flux of mass 3 and 4 antinuclei using the same coalescence model, with $p_0 = 78$ MeV (note that the diagrammatic approach used for the antideuteron case cannot be applied for $A = 4$), and the same hadronic cross sections. Unlike antideuterons for which the $\bar{p}p$ reaction provides a sizable flux, similar reactions (e.g., $\bar{d}p \rightarrow \bar{d}X$) are expected to lead to negligible contributions for heavier antinuclei production. This is because of the expected smallness of the corresponding cross sections, due to the large energy-momentum transfer required to produce antinucleon pairs which would break up the incident (anti)deuterons.

For the tertiary flux of mass 3 antinuclei, the NAR cross section would be large since the restriction to isoscalar transitions discussed for the $\bar{d}$ projectile would not apply (while it would for $^4\bar{\mathrm{He}}$), and a similar procedure as used before for $\bar{d}s$ could be applied. The exercise would be irrelevant, however, on account of the smallness of the expected coalescence cross sections and of the corresponding NAR flux.

The uncertainties associated with these calculations are driven mainly by the uncertainties on the hadronic cross sections, boosted by the coalescence model exponentiation. For the $^3\bar{\mathrm{He}}$ flux, it is estimated that the calculations are accurate within roughly 1 order of magnitude, which is a good enough level of accuracy for the purpose of this work.

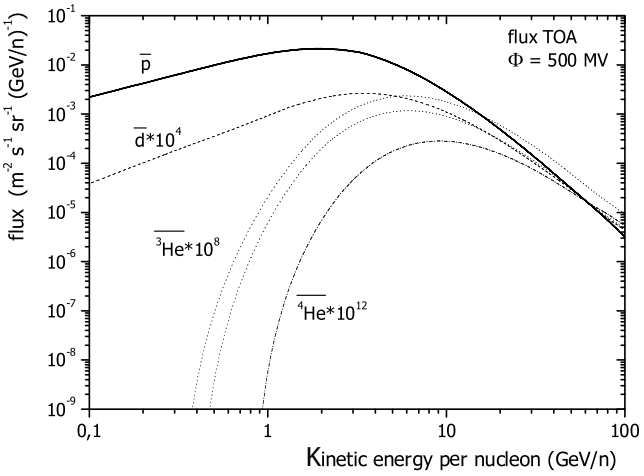

FIG. 15. Galactic flux for $\bar{p}$ (solid line), $\bar{d}$ (dashed), $^3\bar{\mathrm{H}}\mathrm{e}$ (dash-dotted), and $^4\bar{\mathrm{H}}\mathrm{e}$ (dotted) antimatter particles. The lower (respectively upper) dashed line correponds to the case where the ^{3}H production is not taken (respectively taken) into account (see text for details).

D. Summary for the calculated galactic flux

The spectral distributions of the calculated galactic fluxes for mass 1 to 4 antinuclei are displayed in Fig. 15 (full calculation, standard coalescence model). The calculated $\bar{d}$, $^3\bar{\mathrm{H}}\mathrm{e}$, $^4\bar{\mathrm{H}}\mathrm{e}$ fluxes have been multiplied by 10^4, 10^8, 10^{12}, respectively, for presentation purposes. These fluxes are significantly higher than those derived in [20], the difference being mainly due to the larger value of the coalescence momentum derived in the present work, the other smaller differences having been discussed in the text. The roughly twice larger $\bar{d}$ flux between the old and the new coalescence momentum translates into a factor 4 for $^3\bar{\mathrm{H}}\mathrm{e}$ and 8 for $^4\bar{\mathrm{H}}\mathrm{e}$. The upper of the two dashed lines for $^3\bar{\mathrm{H}}\mathrm{e}$ includes the addition of the $\bar{t}$ flux, this latter nucleus decaying into $^3\bar{\mathrm{H}}\mathrm{e}$ with a half life of about 12 years.

V. ATMOSPHERIC PRODUCTION AND PROPAGATION

A CR particle crosses a sizable amount of the Earth's atmosphere before being detected by a balloon borne running experiment. The grammage seen by the CR in this process can be of the same order of magnitude as the grammage seen during its wandering through the Galaxy in a few tens of Myr (typically ~ 10 g/cm^2 at 1 GeV/nuc). The same mechanism which leads to the secondary galactic antimatter flux leads as well to a secondary flux of the same particles via the interaction of CR particles with atmosphere (see [13] for a quantitative comparison).

The CR induced $\bar{p}$ flux in the atmosphere has been measured recently at mountain level, where it is expected to be of purely atmospheric origin [11]. Light antinuclei have also been searched by the same experiment [8]. These atmospheric secondaries will constitute a background for the CR flux of these particles in future experiments. For balloon borne experiments this background, produced in the atmosphere above the detector, must be evaluated to correct the measurements [67]. Besides, atmospheric particles can be trapped by the Earth's magnetic field and detected by satellite experiments. Although they could be separated in principle from the galactic flux on dynamic and kinematic grounds [68], a basic theoretical knowledge of this background is required.

As quoted in the introduction, the phenomenology of the particle production induced by CRs in the atmosphere has been thoroughly investigated recently with the purpose of accounting for the large amount of new data available from recent balloon and satellite measurements. The calculation of the antiproton flux was part of this effort [13]. The latter have been recalculated in the present work with the tertiary (NAR) production taken into account, and extended to the case of $A > 1$ antinuclei production on the same dynamical basis as for the galactic flux, as discussed below. The present results complement and update our previous calculations [13].

A. Antimatter flux

The atmospheric production of antimatter has been calculated along the same lines as in the previous calculations of the atmospheric particle flux by the authors [13,69]. It consists of a 3D Monte Carlo simulation program processing the propagation and interactions of charged particles in the Earth's environment [12,70]. For antinuclei $A \leq 4$, the antimatter production cross sections used in the program have been calculated by means of the same standard coalescence model as described above, using the $\bar{p}$ production cross sections discussed in Sec. II B.

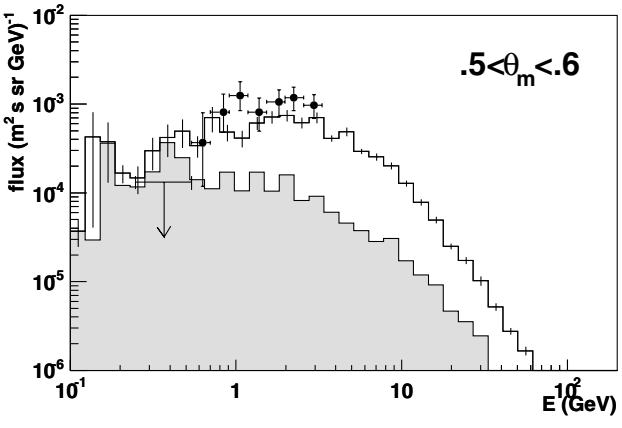

FIG. 16. Atmospheric antiproton flux at mountain altitude (2770 m) measured by BESS Collaboration [11] (at the indicated geomagnetic latitude θ_m), compared with the present calculations. The latter update the results presented in [67]. The gray histogram corresponds to the NAR process, the white histogram showing the full calculations.

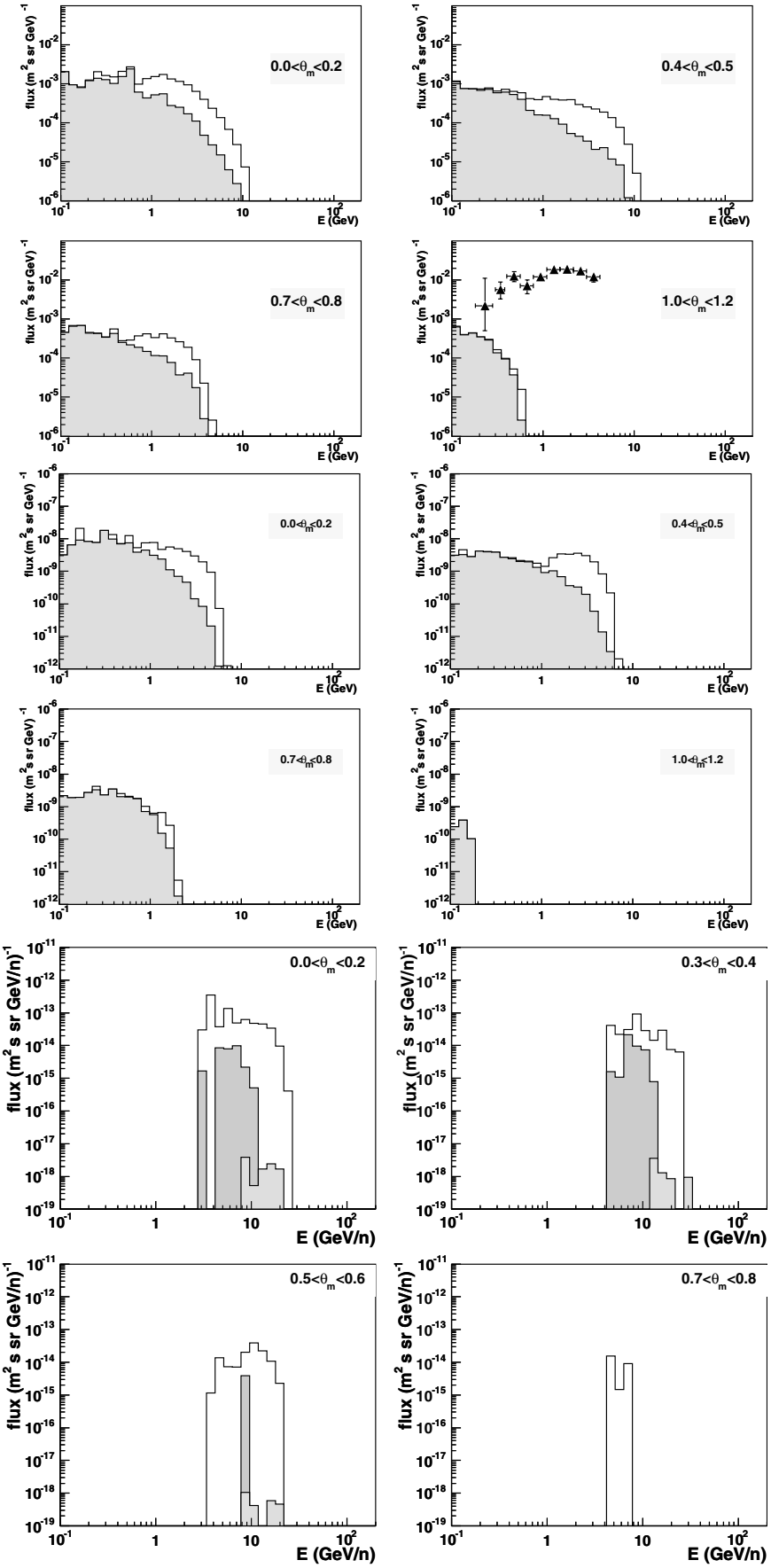

FIG. 17. Calculated fluxes of antimatter nuclei produced in the atmosphere, shown by groups of 4 panels, for $\bar{p}$ (top), $\bar{d}$ (middle), with the full (secondary + tertiary, white histogram) and tertiary only (gray histogram) fluxes shown. The recent experimental $\bar{p}$ data from [80] for the galactic flux at TOA are also shown (full triangles). The lower panel shows the mass 3 and 4 antinuclei fluxes, $\bar{t}$ (dark gray), $^3\bar{\mathrm{He}}$ (white), and $^4\bar{\mathrm{He}}$ (light gray) (bottom). All calculations are for 400 km of altitude, and for the different bins in latitudes between the equator and poles indicated on each individual panel (θ_m is the geomagnetic latitude angle in radian).

In the propagation process, the absorption cross sections for $\bar{p}A$ collisions discussed in Sec. III A 1 above were used, as well as the NAR contributions for the $\bar{p}$ and $\bar{d}$ particles, discussed in Sec. III B.

Figure 16 shows the $\bar{p}$ flux at mountain altitude (2770 m), i.e., deep inside the atmosphere, measured by BESS Collaboration [11], compared to the present calculations. It can be observed that the ratio of the contribution of the tertiary $\bar{p}$ flux (gray histogram on the figure) to the parent secondary component appears to be on the same scale as in the galactic flux, as expected. The overall flux appears to be somewhat ($\approx 20\%$) smaller than the value reported in [13], due to the use of $\bar{p}A$ absorption (total reaction) cross section (see above) smaller in the present calculations than in the previous report. The larger relative flux at small kinetic energies is due to the NAR process, taken into account in the present work while it was not in the previous one. The overall agreement with the data, although not quite as good as in [13], is still fair however.

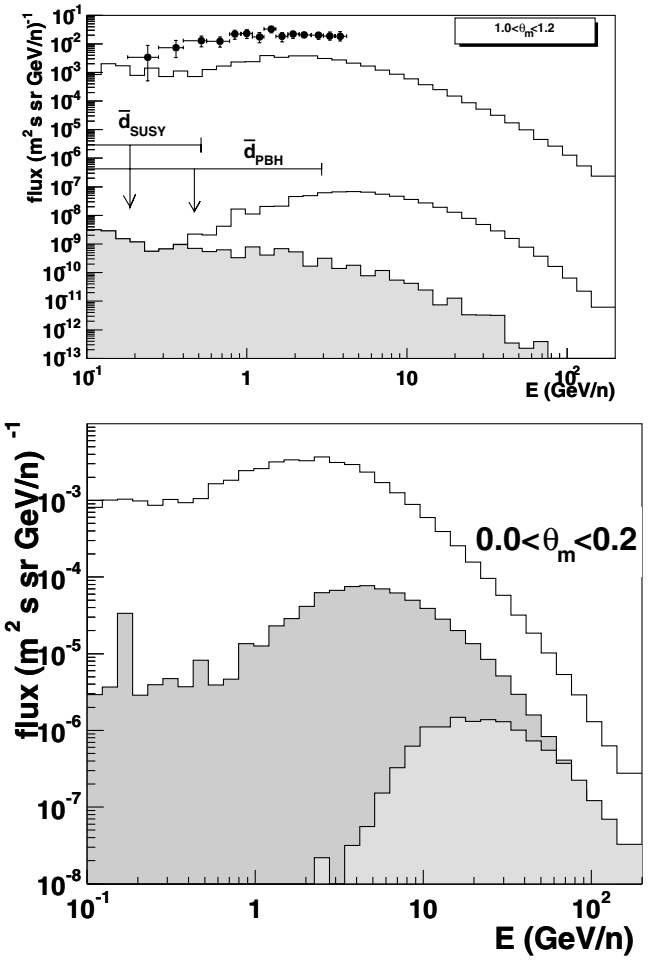

FIG. 18. Top: Calculated atmospheric $\bar{p}$ flux at 38 km of altitude (top histogram) compared with the recent BESS98 measurements [67] (which include both the galactic and the atmospheric components). The lower two histograms correspond to the calculated atmospheric $\bar{d}$ flux in the polar region; the gray histogram shows the tertiary component. The horizontal line labeled $\bar{d}_{\mathrm{SUSY}}$ corresponds to the limit for the $\bar{d}$ flux supersymmetric dark matter annihilation, from [2]. Bottom: Differential atmospheric $\bar{p}$, $\bar{d}(\times 5\ 10^3)$, $^3\bar{\mathrm{He}}(\times 10^6)$ fluxes in the polar region, at 38 km. For this latitude, the $^3\bar{\mathrm{He}}$ and $\bar{t}$ fluxes are identical (identical production cross sections).

Figure 17 shows the downward flux of antimatter nuclei $\bar{p}$, $\bar{d}$, and $\bar{t}$, at 400 km of altitude, induced by CR collisions with atmospheric nuclei, for a set of bins in latitude between the equator and poles [71]. Similar distributions are obtained for the upstream flux, showing that the dominant part of this flux is made of trapped particles [12]. A striking feature of the results is the very large proportion of the flux due to the tertiary component (NAR process), while this fraction was much smaller both for the flux at ground level and for the galactic flux. This originates from the selectivity of the Earth's magnetic field which tends to trap low energy particles more efficiently, the NAR process decreasing the energy of the propagating particle then trapped by the field and confined in the belt. Note that in the polar region where the Earth's field is small, the whole flux is almost totally accounted for by the tertiary component. The same is true for the $\bar{d}$ flux (intermediate panels). The shape of the distributions of the secondary $\bar{p}$ and $\bar{d}$ fluxes are also found to be significantly different from their galactic counterpart (see [72]). In particular, the atmospheric secondary particle spectra appear to have their maximum at different energies than galactic particles. All these features are due to the dynamics of the particles in the Earth's magnetic field, which may induce considerable distortion of the primary particle spectra [71]. In Fig. 18 (top panel), for the polar latitudes, the $\bar{p}$ flux compared with the TOA measurements by BESS shows that this atmospheric background is negligible at the considered satellite altitude for energies $T \gtrsim 0.5$ GeV. At lower energies, however, the data and the atmospheric flux seem to converge towards close values.

Figure 18, lower panel, shows the calculated spectral distributions for mass 3 and 4 antinuclei. The typical structure has the same origin as for lighter antinuclei: the spectrum is limited by the rise of the particle production cross section driven by the production threshold (itself rising with the mass of the produced particle), on the lower side. The upper energy limit is set by the trapping conditions. For these fluxes the NAR contributions have not been included. Dynamically, the same considerations as given in Sec. IV C concerning the NAR process are valid as well for atmospheric particles. However, as seen above, the expected NAR effect is much larger for atmospheric than for galactic fluxes. Including this process would somewhat weaken the high energy component and strongly populate the low energies (empty on the figure). But the induced change (increase of the overall flux), although significant at the considered order of magnitude, would not modify the conclusion, the overall flux being vanishingly small.

TABLE III. Expected count rates for light antinuclei in the AMS experiment, for 3 years of effective counting [46,71], as described in the text.

Particles	$\bar{p}$	$\bar{d}$	$^3\bar{\mathrm{He}}$	$^4\bar{\mathrm{He}}$
Galactic rate	10^6	15	10^{-3}	10^{-7}
Atmospheric rate	$5\ 10^5$	3	10^{-4}	$5\ 10^{-9}$

VI. COUNTING STATISTICS FOR LIGHT ANTIMATTER NUCLEI AT SATELLITE ALTITUDE

The forthcoming search experiments for primordial antimatter will need some estimated values of the expected secondary galactic and atmospheric flux for the investigated particles, to be compared with the experimental results. The secondary fluxes of antimatter particles calculated above have been energy integrated over the energy range 0.1–100 GeV per nucleon and over the Alpha Magnetic Spectrometer (AMS) orbit taking into account the effects of the geomagnetic cutoff and using an approximate acceptance of 0.5 m^2sr for the AMS. The results are given in Table III. The resulting counting statistics to be expected are of the order of 10^6, 20, 10^{-3}, and 10^{-7} particles per year, for $\bar{p}$, $\bar{d}$, $^3\bar{\mathrm{He}}$, and $^4\bar{\mathrm{He}}$, respectively. Clearly, the rates for mass 3 and 4 antinuclei are negligibly small even at the scale of very small statistics. Note however that a $^4\bar{\mathrm{He}}$ candidate event would have the largest probability of being a misidentified background $^3\bar{\mathrm{He}}$ particle.

For the AMS experiment, a more accurate estimate of these numbers will be obtained with the processing of these fluxes in the AMS simulation program, taking into account the identification capability of the instrument. The work is under way and the results will be reported later.

VII. SUMMARY

This work has provided new calculations of the light antinuclei $\bar{p}$, $\bar{d}$, $^3\bar{\mathrm{He}}$, $^4\bar{\mathrm{He}}$ fluxes produced by CR collisions on the ISM in the Galaxy, and the first calculations of the fluxes produced by CRs in the atmosphere for the same particles. For the $\bar{d}$ flux, a new production channel $\bar{p}p \rightarrow \bar{d}X$ has been included in the calculations and was shown to contribute significantly to the total flux. The cross sections involved in the calculations were based to a large extent on existing accelerator data. The results are found significantly different from previous calculations. The calculated fluxes above 0.5–1 GeV/n are estimated to be reliable within a factor of 2 for the $\bar{d}$ flux, and within 1 order of magnitude for mass 3 antinuclei. The calculated flux in the low energy range, below 0.5 GeV/n, suffers larger uncertainties mainly because of the lack of experimental data. The calculated $\bar{d}$ flux appears to be marginally detectable by the AMS experiment mainly because it will have to be discriminated against a large background of $\bar{p}s$ and electrons.

A further step will consist of using the calculated $\bar{d}$ flux as an input to the AMS02 spectrometer simulation together with the other particles with the same electric charge ($\bar{p}$, electrons) with their respective galactic fluxes, and discriminating the $\bar{d}s$ from the other particles by means of spectrometers, in order to evaluate the capacity of the experiment to achieve the measurement of this flux.

ACKNOWLEDGMENTS

The authors are indebted to P. Salati and R. Taillet for several enlightening discussions on the subject. The diffusion model calculations are based on a code originally written by P. Salati.

APPENDIX: INELASTICITY IN COMPOSITE PARTICLE SCATTERING

First, let us consider the system for incident deuterons rather than antideuterons. The result will be easily extended to $\bar{d}$ later. Qualitatively the effect of the small dissociation energy of the deuteron, or of any nucleus or other quantal system with small binding energy, is to make the collision highly diffractive because of the strong absorption induced by the large dissociation cross section of the deuteron. Because of this larger collision opacity, the inelastic collisions on nuclei will be more peripheral than they would be for an incident nucleon, for example. For the same reason the angular distribution will be more forward peaked, partly because of the fragility of the projectile which limits the range of momentum transfer to low values, as explained below. But this does not imply that they would have a smaller cross section. In fact, it can be shown that, to the contrary, the inelastic collision cross section induced by a composite nuclear projectile is expected to be larger than for incident nucleons. This is also supported by the existing data.

In the case of dp collisions on a nucleon target, however, the system is rather transparent and the diffractive effect can only be loosely referred to, the forward peaking of the cross section being induced mainly by the deuteron form factor. As discussed below, the latter is broader in the momentum space and the resulting angular distribution more forward peaked, which means that only low momentum transfers are allowed in the scattering process.

All the above arguments apply to the case of incident antideuterons whose collisions are made even more diffractive than for incident deuterons by the stronger absorption induced by the annihilation channels. The following arguments apply equally well to both cases.

In the type of collision considered here, the incident $\bar{d}$ excites the ISM nucleon into a resonancelike state with mass M_X. The process is dominantly diffractive, characterized by small momentum transfer and peripheral character. The hit nucleon can as well be bound inside a (ISM) nucleus.

The transition amplitude $F(t)$ (t 4-momentum transfer) for such a reaction can be most conveniently described for the present pedagogical purpose, in the single scattering limit of the Glauber multiple scattering approach for the collisions of composite systems [73,74], namely, the impulse approximation, in terms of the form factors of the interacting systems $G_p(t)$, $G_t(t)$ and of the interaction term $v(t)$. The full Glauber amplitude can be written as

$$F(t) = \int d^2b e^{i\vec{q}\cdot\vec{b}} \langle \Psi_p \phi_t^* | \Gamma(b, s_p, s_t) | \Psi_p \phi_t \rangle \qquad (13)$$

where Ψ_p, $\phi_t(\phi_t^*)$ are the projectile and target ground (excited) state wave functions, respectively; b, s_p, and s_t, the impact parameter variables; and $\Gamma(b, s_p, s_t) = 1 - e^{i\sum \chi_j}$ the (Glauber) profile function of the collision system, with χ_j being the individual phase shift functions of the elementary constituents [75], namely, nucleons for a nuclear system [73], constituent quarks for a subnucleon system [76], or both [77]. This later relation is the foundation of the Glauber approximation and leads to the well-known multiple scattering series of the scattering amplitude.

A classical illustration of the correctness of the Glauber approach is precisely the application to the total deuteron cross section on proton, for which the above series for the case of elastic scattering using the optical theorem leads to [78]

$$\sigma_{\rm tot}(dp) \approx \sigma(pp) + \sigma(np) - (\text{2nd order shadowing term}).$$

In the single scattering approximation, i.e., the Plane Wave Impulse Approximation (PWIA) (or Chou-Yang model for hadron collisions), the elastic scattering amplitude takes the very simple form

$$F(t) \sim A_p A_t G_p(t) G_t(t) v(t) \qquad (14)$$

where the numbers of constituents of the two systems A_p and A_t originate from the normalization of the ground state wave function [73,74]. From this relation, it can be shown straightforwardly by simple application of the optical theorem, that the total reaction cross section is proportional to the product of the number of constituents times the elementary total cross section between constituents $\sigma_{\rm tot} = A_p A_t \sigma_0$. This is the additive quark model for hadron-hadron collisions [79].

The derivation for the inelastic $Dp \to DX$ cross section goes through identical steps with the only difference being that the proton final state is an excited state rather than the ground state, and the product of the initial and final proton wave functions in the relation above, which describes the ground state density in the case of elastic scattering, then becomes a transition density describing the excited nucleon state $\delta\rho(r)$ instead of the ground state density $\rho(r)$.

A similar relation applies for inelastic scattering. In that case, one (or both) of the form factors involved describe the excited state, namely $F(t) \sim A_p A_t G_p(t) v(t) \delta_t(t)$.

Therefore the expected inelastic $Ap \to AX$ cross section, A being a composite system such as the deuteron d, is expected to be larger than its counterpart in nucleon-nucleon scattering $pp \to pX$.

This result is confirmed by the experimental data from [53] (see also [75]) where a larger cross section for $dn \to d(p\pi^-)$ than for $pn \to p(p\pi^-)$ was measured (see Table 2 and Fig. 6 in [53]; see also [57]).

[1] F. Donato *et al.*, Astrophys. J. **563**, 172 (2001).
[2] F. Donato, N. Fornengo, and P. Salati, Phys. Rev. D **62**, 043003 (2000).
[3] A. Barrau *et al.*, Astron. Astrophys. **398**, 403 (2003).
[4] A. Barrau *et al.*, Astron. Astrophys. **388**, 676 (2002); Phys. Lett. B **551**, 218 (2003); A. Barrau and N. Ponthieu, Phys. Rev. D **69**, 105021 (2004).
[5] M. Aguilar *et al.*, Phys. Rep. **366**, 331 (2002).
[6] M. Simon *et al.*, in *Proceedings of the 28th International Cosmic Ray Conference, Tsukuba (Japan), 2003*, edited by T. Kajita, Y. Asaoka, A. Kawachi, Y. Matsubara, and M. Sasaki.
[7] T. Yoshida *et al.*, in Ref. [6].
[8] H. Fuke *et al.*, in Ref. [6], Vol. l4, p. 1797.
[9] S. Haino *et al.*, Phys. Lett. B **594**, 35 (2004).
[10] M. Boezio *et al.*, Astrophys. J. **487**, 415 (1997).
[11] T. Sanuki *et al.*, Phys. Lett. B **577**, 10 (2003).
[12] L. Derome *et al.*, Phys. Lett. B **489**, 1 (2000); L. Derome and M. Buénerd, Phys. Lett. B **521**, 139 (2001).
[13] C. Y. Huang, L. Derome, and M. Buénerd, Phys. Rev. D **68**, 53008 (2003).
[14] R. Duperray, C. Y. Huang, K. Protasov, and M. Buénerd, Phys. Rev. D **68**, 094017 (2003).
[15] R. Arsenescu *et al.*, Nucl. Phys. **A661**, 177c (1999).
[16] NA44 Collaboration, J. Simon-Gillo *et al.*, Nucl. Phys. **A590**, 483c (1995); F. Stoffel, Ph.D. thesis, University of Bern, 1997.
[17] NA44 Collaboration, I. G. Bearden *et al.*, Nucl. Phys. **A661**, 55c (1999).
[18] E864 Collaboration, G. Van Buren *et al.*, Nucl. Phys. **A661**, 391c (1999).
[19] NA52 Collaboration, G. Ambrosini *et al.*, Phys. Lett. B **417**, 202 (1998).

[20] P. Chardonnet, J. Orloff, and P. Salati, Phys. Lett. B **409**, 313 (1997).

[21] D. Maurin, F. Donato, R. Taillet, and P. Salati, Astrophys. J. **555**, 585 (2001); D. Maurin, R. Taillet, and F. Donato, Astron. Astrophys. **294**, 1039 (2003).

[22] S. T. Butler and C. A. Pearson, Phys. Rev. **129**, 836 (1963); A. Shwarzshild and C. Zupančic, Phys. Rev. **129**, 854 (1963).

[23] L. P. Csernai and J. I. Kapusta, Phys. Rep. **131**, 223 (1986).

[24] J. Barrette *et al.*, Phys. Rev. C **50**, 1077 (1994).

[25] N. Saito *et al.*, Phys. Rev. C **49**, 3211 (1994).

[26] S. Nagamiya *et al.*, Phys. Rev. C **24**, 971 (1981).

[27] V. V. Abramov *et al.*, Sov. J. Nucl. Phys. **45**, 845 (1987).

[28] A. Bussière *et al.*, Nucl. Phys. **B174**, 1 (1980); W. Bozzoli *et al.*, Nucl. Phys. **B144**, 317 (1978).

[29] J. W. Cronin *et al.*, Phys. Rev. D **11**, 3105 (1975).

[30] T. A. Armstrong *et al.*, Phys. Rev. C **59**, 2699 (1999).

[31] NA44 Collaboration, I. G. Bearden *et al.*, Phys. Rev. Lett. **85**, 2681 (2000).

[32] E878 Collaboration, M. G. Bennett *et al.*, Nucl. Phys. **A590**, 491c (1995).

[33] D. E. Dorfan *et al.*, Phys. Rev. Lett. **14**, 1003 (1965).

[34] B. Alper *et al.*, Phys. Lett. B **46**, 265 (1973).

[35] M. G. Albrow *et al.*, Nucl. Phys. **B97**, 189 (1975).

[36] W. M. Gibson *et al.*, Lett. Nuovo Cimento Soc. Ital. Fis. **21**, 189 (1978).

[37] V. V. Abramov *et al.*, Z. Phys. C **24**, 205 (1984).

[38] D. Hardtke *et al.*, Nucl. Phys. **A698**, 671c (2002).

[39] V. M. Kolybasov and Yu. N. Sokol'skikh, Sov. J. Nucl. Phys. **55**, 1148 (1992).

[40] R. Duperray, Derome, M. Buénerd, A. Yu. Voronin, and K. Protasov, Eur. Phys. J. A **16**, 27 (2003); R. Duperray, K. Protasov, and A. Yu. Voronin, Eur. Phys. J. A **18**, 597 (2003).

[41] J. C. M. Armitage *et al.*, Nucl. Phys. **B150**, 87 (1979).

[42] Yu. M. Antipov, Phys. Lett. B **34**, 164 (1971); F. Binon *et al.*, Phys. Lett. B **30**, 510 (1969).

[43] A. N. Kalinovski, M. V. Mokhov, and Yu. P. Nikitin, *Passage of High Energy Particles through Matter* (AIP, New York, 1989), Chap. 3.

[44] Yu. M. Antipov *et al.*, Nucl. Phys. **B31**, 235 (1971); Sov. J. Nucl. Phys. **12**, 171 (1971).

[45] N. K. Vishnevsky *et al.*, Yad. Fiz. **20**, 694 (1974) [Sov. J. Nucl. Phys. **20**, 371 (1974)].

[46] R. Duperray, Ph.D. thesis, Université J. Fourier, Grenoble (France) [Institution Report No. LPSC/04-37 (unpublished)].

[47] L. C. Tan and L. K. Ng, J. Phys. G **9**, 227 (1983).

[48] G. Bendiscioli and D. Kharzeev, Riv. Nuovo Cimento **17**, 1 (1994).

[49] S. P. Denisov *et al.*, Nucl. Phys. **B31**, 253 (1971); F. Binon *et al.*, Phys. Lett. B **31**, 230 (1970).

[50] Yu. P. Gorin *et al.*, Sov. J. Nucl. Phys. **14**, 76 (1972); Phys. Lett. B **34**, 164 (1971).

[51] C. Furget, M. Buénerd, and P. Valin, Z. Phys. C **47**, 377 (1990); C. Furget, Ph.D. thesis, Université de Grenoble [Institution Report No. ISN/89-93, 1990 (unpublished)].

[52] J. Banaigs *et al.*, Phys. Lett. B **45**, 535 (1973).

[53] G. Goggi *et al.*, Nucl. Phys. **B161**, 14 (1979).

[54] H. P. Morsch *et al.*, Phys. Rev. Lett. **69**, 1336 (1992).

[55] J. Allaby *et al.*, Nucl. Phys. **B52**, 316 (1973); E. W. Anderson *et al.*, Phys. Rev. Lett. **25**, 699 (1970).

[56] R. Baldini-Celio *et al.*, Nucl. Phys. **B107**, 321 (1976).

[57] A. Baldini *et al.*, Landolt-Börnstein New Series Vol. I/12b (Springer-Verlag, Berlin, 1988).

[58] E. W. Anderson *et al.*, Phys. Rev. Lett. **19**, 198 (1967); M. A. Abolins *et al.*, Phys. Rev. Lett. **25**, 126 (1970).

[59] H. M. Fried and T. K. Gaisser, Phys. Rev. D **6**, 2560 (1972); P. M. Fishbane *et al.*, Phys. Rev. D **9**, 3083 (1974); L. C. Tang and L. K. Ng, J. Phys. G **9**, 227 (1983).

[60] F. C. Jones, A. Lukasiak, V. Ptuskin, and W. Webber, Astrophys. J. **547**, 264 (2001).

[61] W. R. Webber *et al.*, Astrophys. J. **457**, 435 (1996).

[62] M. Simon, A. Molnar, and S. Roesler, Astrophys. J. **499**, 250 (1998).

[63] I. V. Moskalenko *et al.*, Astrophys. J. **565**, 280 (2002).

[64] M. Antinucci *et al.*, Lett. Nuovo Cimento Soc. Ital. Fis. **6**, 121 (1973).

[65] L. Bergström, J. Edsjö, and P. Ullio, Astrophys. J. **526**, 215 (1999).

[66] T. K. Gaisser *et al.*, *26th ICRC, Salt Lake City, 1999, OG-1.1.19.*

[67] S. T. Maeno *et al.*, Astropart. Phys. **16**, 121 (2001).

[68] C. Störmer, *The Polar Aurora* (Clarendon Press, Cambridge, 1955).

[69] B. Baret, L. Derome, C. Y. Huang, and M. Buénerd, Phys. Rev. D **68**, 053009 (2003).

[70] Yong Liu, L. Derome, and M. Buénerd, Phys. Rev. D **67**, 073022 (2003).

[71] B. Baret, Ph.D. thesis, Université Joseph Fourier, Grenoble, France [Institution Report No. LPSC/04-70, 2004 (unpublished)].

[72] B. Baret *et al.*, in Ref. [6].

[73] V. Franco and G. K. Varma, Phys. Rev. C **18**, 349 (1978).

[74] M. Buénerd and C. Furget, Phys. Rev. D **41**, 103 (1990).

[75] G. Alberi and G. Goggi, Phys. Rep. **74**, 1 (1981).

[76] D. R. Harrington and A. Pagnamenta, Phys. Rev. **173**, 1599 (1968).

[77] S. Forte, Nucl. Phys. **A467**, 665 (1987).

[78] V. Franco and R. J. Glauber, Phys. Rev. **142**, 1195 (1966).

[79] H. Lipkin and F. Scheck, Phys. Rev. Lett. **16**, 71 (1966); J. J. J. Kokkedee, *The Quark Model* (WA Benjamin, New York, 1969).

[80] Y. Asaoka *et al.*, Phys. Rev. Lett. **88**, 051101 (2002).